POLITECNICO
MILANO 1863

SCUOLA DI INGEGNERIA INDUSTRIALE
E DELL'INFORMAZIONE

Characterization of Fragmentation Events in Near Earth Environment exploiting Conjunction Analysis

Tesi di Laurea Magistrale in
Space Engineering - Ingegneria Spaziale

Author: **Paola Grattagliano**

Student ID: 996403
Advisor: Prof. Marco Felice Montaruli
Co-advisors: Prof. Pierluigi Di Lizia
Academic Year: 2022-2023

Abstract

The population of Resident Space Objects is increasing exponentially, especially in the lower Earth orbits. These host various kinds of debris, which continuously pose a major problem for the orbiting satellites, on the one hand risking to disable a mission and on the other potentially causing chains of events able to generate further objects. In this regard, fragmentation events (eg. collisions, explosive break-ups, wearing of materials...) represent a criticality, currently being the dominant source of space debris. The aim of the following research is to improve an existing tool able to characterize a fragmentation event. Its epoch is the expected result of the implemented routine. This would allow to plan further observations and soon predict the debris proliferation. To achieve this, the analysed event is treated as a collision between the primary object (parent) and the resulting fragment. This analogy allows to compute the Probability of Collision (PoC) between the two objects. The result is analysed as a series of values in time, and when the maximum value is identified, the corresponding Time of Closest Approach is stored as a possible fragmentation epoch. Another typical Conjunction Analysis (CA) criterion, the Mahalanobis distance, is then applied to determine a single estimated epoch as the output. In this routine, the use of Gaussian Mixture Models (GMM) is exploited as a method of uncertainty propagation. The result of this addition with respect to existent methods of CA is expected to be a more robust computation of the PoC. GMM allow in fact to better capture the non-linearities of the propagation model, which usually appear after many orbital periods and are hardly well represented if the initial uncertainty is assumed Gaussian. To test the application of the method as well as to validate the use of GMM, a test case is conducted for an anti-satellite test involving the breakup of Cosmos 1408, happened in November 2021. The result of the work is a new metric of characterization of these critical events, with a big advantage: it requires solely a single orbital state among all produced fragments and one ephemeris of the primary object.

Keywords: Space Debris, Conjunction Analysis, Fragmentations, Collision Probability, Gaussian Mixture

Abstract in lingua italiana

La popolazione degli oggetti residenti nello spazio sta aumentando in modo esponenziale, specialmente nelle orbite terrestri più basse. Queste ospitano vari tipi di detriti, che costituiscono costantemente un problema significativo per i satelliti in orbita. Da un lato c'è il rischio di compromettere una missione, mentre dall'altro l'eventualità di causare catene di eventi capaci di generare ulteriori oggetti. A questo proposito, gli eventi di frammentazione (che includono collisioni, rotture esplosive, usura dei materiali...) rappresentano una criticità, essendo attualmente la fonte dominante di detriti spaziali. Lo scopo della seguente ricerca è migliorare un *tool* esistente in grado di caratterizzare un evento di frammentazione. La stima dell'epoca di tale evento è il risultato atteso della *routine* implementata. Ciò consentirebbe di pianificare ulteriori osservazioni e prevedere presto la proliferazione dei detriti. A tale scopo, l'evento analizzato è trattato come una collisione tra l'oggetto originario (genitore) e il frammento risultante. Questa analogia consente di calcolare la PoC tra i due oggetti. Il risultato è analizzato come una serie di valori nel tempo, e quando viene identificato il massimo, l'istante di minimo avvicinamento corrispondente viene registrato come possibile epoca di frammentazione. Un altro criterio tipico della CA, la distanza di *Mahalanobis*, è poi applicato per determinare una singola stima dell'epoca in output. In questa *routine* le GMM sono impiegate come metodo di propagazione dell'incertezza. Il risultato di questa aggiunta, rispetto a metodi già esistenti nella CA, sarebbe un calcolo più robusto della PoC. Le GMM consentono infatti di catturare meglio le non-linearità del modello di propagazione, che generalmente si manifestano dopo molti periodi orbitali e sono difficili da rappresentare in maniera adeguata se l'incertezza iniziale viene assunta come Gaussiana. Per eseguire la simulazione del metodo e per validare l'applicazione delle GMM, viene condotto un *test case* su un test anti-satellite che ha coinvolto la frammentazione di Cosmos 1408, avvenuta nel novembre 2021. Il risultato del lavoro è una nuova metrica per caratterizzare questi eventi critici, con un grande vantaggio: richiede esclusivamente un singolo stato orbitale tra tutti i frammenti prodotti e una effemeride dell'oggetto originario.

Parole chiave: Detriti Spaziali, Analisi di Congiunzione, Frammentazioni, Probabilità di Collisione, Gaussian Mixture

Ringraziamenti

Sono fortemente grata al mio relatore, il Professore Marco Felice Montaruli, per avermi pazientemente aiutato con i suoi consigli e supportata durante lo svolgimento della tesi, con umanità e professionalità. Ringrazio calorosamente anche il mio correlatore, il Professor Pierluigi Di Lizia, per avermi dato l'opportunità di svolgere questa tesi, per essere sempre stato disponibile e per avermi saputo entusiasmare alla ricerca.
Desidero ringraziare chi più di tutti mi è stato accanto: la mia famiglia qui a Milano, mamma Teresa, papà Michele e il fratell(in)o Nic. Mi avete spronato nei momenti di difficoltà, avete provveduto al mio stare bene quando io ero troppo impegnata nello studio matto di questi anni, ma soprattutto avete sopportato il mio carattere *bello ma tremendo* volendomi sempre bene. Grazie a tutto il lato pugliese della famiglia: grazie ai Nonni, agli Zii, a mia cugina che è come una sorella per me, e anche a chi purtroppo non c'è più. Ho portato nel cuore ognuno di voi durante questi anni.
Ringrazio poi il gruppo di amici che mi hanno accompagnato e motivato in questo viaggio, e davvero lo hanno reso incredibile: il gruppone *Biblioteam*. Ricorderò le giornate passate insieme a studiare accampati in Bovisa, le lezioni online, tra Covid e mascherine, ma sempre in compagnia. Siete troppi per essere ringraziati singolarmente, ma non sarebbe stato lo stesso senza di voi, e desidero davvero che questi rapporti rimangano negli anni avvenire. Grazie ad Annaky, Fabrizio, Lerp e Richi, siete voi con cui ho stretto subito amicizia. Grazie ai meccanici, sicuramente più sani di noi aerospaziali, Fabri, Umberto e Elisabetta, Luca. Grazie anche a tutti gli altri per le gite tra gli scorpioni, le camminate in montagna, gli episodi di *Attack on Titan* in compagnia. Grazie agli *Enceladiani*, siete stato il team perfetto. Vorrei poi salutare tutte le persone che ho conosciuto grazie a PoliSpace. Entrare a far parte dell'associazione mi ha aperto opportunità di crescita e di viaggi incredibili, di sfide pratiche con cui confrontarmi. Vi auguro il meglio per il futuro, e per il lancio tanto atteso del Cubesat. *Alatis Grave Nihil*!
Ringrazio tutti gli amici storici di Milano, per l'affetto dimostrato durante questi anni. Ringrazio le mie sorelle non letterali, Alice, Beatrice e Francesca. Vi voglio bene. Ringrazio Silvia, sei stata sempre di supporto, anche a distanza. Ringrazio gli altri *bimbi di Albina* e per le vacanze passate insieme: Fra e Jack con le sue pazze giornate in campagna.

Ringrazio il gruppo ritrovato dei compagni delle elementari, e ringrazio tutti gli amici di famiglia, tra cui Giulia, Federica, Lilli e Francesca.
Ringrazio, infine, Luca. Sono grata di averti conosciuto proprio durante questo percorso. Grazie a te per l'amore, per avermi sempre supportato, per le esperienze fatte insieme e che ci hanno fatto crescere. Anche a te congratulazioni, ti auguro sempre le cose più belle.

Paola (o Pleng, splEng., Sbronz e tanti altri)

Contents

Acronyms

ASAT Anti-Satellite.

CA Conjunction Analysis.
CAM Collision Avoidance Maneuvers.

ECI Earth-Centered Inertial.
ET Ephemeris Time.

FRED FRagmentation Epoch Detector.

GME Gaussian Mixture Element.
GMM Gaussian Mixture Models.

HBR Hard-Body Radius.

IOD Initial Orbit Determination.

LEO Low Earth Orbit.

MOID Minimum Orbital Intersection Distance.

OD Orbit Determination.

PDF Probability Density Function.
PoC Probability of Collision.

RAAN Right Ascension of the Ascending Node.
ROD Refined Orbit Determination.
RSO Resident Space Object.

SBM Standard Breakup Model.
SGP4 Simplified General Perturbations model 4.
SST Space Surveillance and Tracking.

T2O Track-to-Orbit.
T2T Track-to-Track.

TCA Time of Closest Approach.
TEME True Equator Mean Equinox.
TLE Two-Line Element.
TOF Time of Flight.

UP Uncertainty Propagation.
UT Unscented Transform.
UTC Coordinate Universal Time.

List of Figures

List of Tables

List of Symbols

Variable	Description	Unit measure
B^*	Drag coefficient	km^{-1}
N_f	Number of elements in the fragment GMM	/
N_i	Generic number of elements in the GMM	/
N_{orb}	Number of periodicities in the analysis window	
N_p	Number of elements in the parent GMM	/
$\boldsymbol{P}$	Covariance matrix	km^2, $(km/s)^2$
$_P$	Subscript related to primary object in a collision	/
$\boldsymbol{P}_C$	Combined covariance matrix	km^2, $(km/s)^2$
P^c	Collision probability	/
P^c_{prod}	Collision probabilities product in time	/
P^c_{ratio}	Collision probabilities logarithmic ratio	/
P^c_{tot}	Cumulative collision probability in time	/
P^c_1	Highest collision probability	/
P^c_2	Second highest collision probability	/
$\boldsymbol{P}_i$	i-th covariance matrix of the GMM	km^2, $(km/s)^2$
$\boldsymbol{P}^p_{old}$	Parent covariance matrix (according to [1])	km^2, $(km/s)^2$
$\boldsymbol{P}^p$	Parent covariance matrix (according to [2])	km^2, $(km/s)^2$
$_S$	Subscript related to secondary object in a collision	/
T	Orbital period	s
V	Integration volume	km^3
W	Unscented Transform weights	/
$\boldsymbol{\mathcal{Y}}$	Propagated sigma point	km, km/s
a	Semi-major axis	km
$\boldsymbol{a}_p$	Perturbing acceleration	km/s^2

Variable	Description	Unit measure
d_M	Mahalanobis distance	/
e	Eccentricity	/
^{f}	Superscript related to fragment object	/
$_g$	Subscript related to Gaussian	/
i	Index referring to the periodicity in the analysis window	/
i	Inclination	deg
i_f	Index referring to the fragment GMM elements	/
$\tilde{i}_f$	Index referring to the fragment GMM element with minimum d_M	/
i_p	Index referring to the parent GMM elements	/
$\tilde{i}_p$	Index referring to the parent GMM element with minimum d_M	/
^{p}	Superscript related to parent object	/
$\boldsymbol{r}$	Position vector	km
$_{rel}$	Subscript related to relative quantity	/
$_s$	Subscript referring to a sample	/
t	Epoch	s (J2000)
t_a	Epoch associated to the alert of the fragmentation event	s (J2000)
t_i	Time steps in the analysis windows (marking the periodicities)	s (J2000)
t_{i_p,i_f}	Epoch of passage through the MOID	s (J2000)
t_{od}	Epoch at which the Orbit Determination is performed	s (J2000)
t_{tle}	Epoch associated to the parent TLE	s (J2000)
t_0	Fragmentation event true epoch	s (J2000)
$\tilde{t}_0$	Estimated fragmentation event epoch	s (J2000)
$_{tle}$	Subscript related to the TLE information	/
$\boldsymbol{v}$	Velocity vector	km
$\boldsymbol{x}$	State vector	km, km/s
(x^e, y^e, z^e)	Position coordinates in the encounter reference frame	km
(x^u, y^u, z^u)	Position coordinates in the principal axes frame	km

Variable	Description	Unit measure
$\{\boldsymbol{x}, \boldsymbol{P}\}$	Gaussian multivariate distribution of mean $\boldsymbol{x}$ and covariance $\boldsymbol{P}$	km, km/s, km^2, $(km/s)^2$
α_i	Weight of the i-th element in the GMM	/
ε	Time error of estimated epoch	s, min (J2000)
μ	Earth gravitational parameter	km^3/s^2
$\boldsymbol{\mu}_i$	i-th mean state vector of the GMM	km, km/s
Ω	Right Ascension of the Ascending Node	deg
ω	Argument of pericentre	deg
σ	Standard deviation	km, km/s
$\boldsymbol{\chi}$	Sigma point	km, km/s

1 | Introduction

1.1. Near-Earth Debris Environment

The ongoing rise in the number of Resident Space Objects (RSOs) in orbit is a significant concern in the advancement of space services, particularly within the Low Earth environment. The Kessler effect [3] is inevitably already in action, causing a chain reaction and increase in frequency of future collisions, as the number of debris has reached a sort of "tipping point". In particular, these debris may be defined as *manmade objects and their fragments launched into space, inactive nowadays and not serving any useful purpose* [4]. According to ESA 2023 most recent report on the Space Environment [5], the objects which can be traced back to a launch event and identifiable in nature can thus be classified:

- Payloads (PL)
- Payload mission related objects (PM)
- Payload fragmentation debris (PF)
- Payload debris (PD)
- Rocket bodies (RB)
- Rocket mission related objects (RM)
- Rocket fragmentation debris (RF)
- Rocket debris (RD)

.

The rest of the objects, which are unidentifiable in origin and nature, is identified as UI (UnIdentified). Hence, the exponential growth of the population is clearly visible in Figure 1.1:

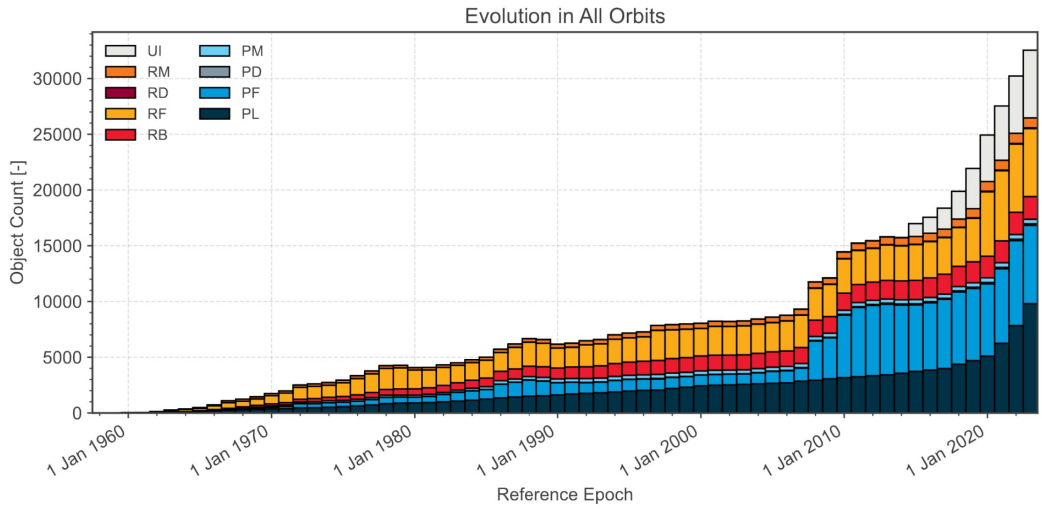

Figure 1.1: Evolution of Space debris over time in all orbits. The two jumps in the population correspond to the two major fragmentation events that have occurred [6]. Image source: [5].

The latest data regarding the amount of orbiting non functioning objects are provided by ESA Space Debris Office. About 15,880 satellites have been placed into Earth orbit in more than 60 years of activities, causing now the presence of 36,500 debris with dimensions over 10 cm, 1,000,000 debris with dimensions between 1 cm and 10 cm and 130 million debris with smaller dimensions [7].
It is clear that this population poses a threat to both future and current missions. The impact with a functioning satellite may end its operational life or parts of it, causing scientific and economic damage to any mission, and on the other hand can generate additional fragments (triggering the chain effect). The latter consequence is particularly critical: fragmentation events are in fact currently the dominant source of space debris [5].

1.2. SST and Catalog Maintenance

To address the challenges described in Section 1.1, different activities are carried out with the aim of cataloguing and characterizing part of the orbiting RSOs, monitoring the fragmentation events, and applying countermeasures to the problem. At European level, one of the greatest contribution in terms of technology is provided by ESA Space Surveillance and Tracking (SST) segment, comprising a network of systems aimed to detect, catalogue and predict the orbits of these objects. The core activity of an SST system is the build up and maintenance of a data catalog which contains information on all

detected objects [8]. This inventory is updated through the observation data acquired by the sensors and processed by the "processing pipeline" of SST itself [9]. Once the catalog is produced and can be maintained, the segment is able to provide further applications: from the automatic assessment of potential collisions between tracked objects and consequent warning to the operators, to risk assessment of uncontrolled re-entry of man-made space objects and detection and characterisation of in-orbit fragmentations.
The Space-Track database, provided by the United States Space Force Space Domain Awareness unit, is publicly available. It contains around 25,000 objects currently around the Earth [10], whose orbits are available in Two-Line Element (TLE) format. These are particularly accessible and in fact constitute one of the main inputs for the routine tested in the aforementioned research work.
As previously stated, fragmentation events constitute the greatest contribution to space pollution and are therefore expected to increase the complexity of catalogs build-up and maintenance activities. Normally the steps involved in the construction of the catalog and its maintenance can be summarized by the chain of blocks represented in Figure 1.2.

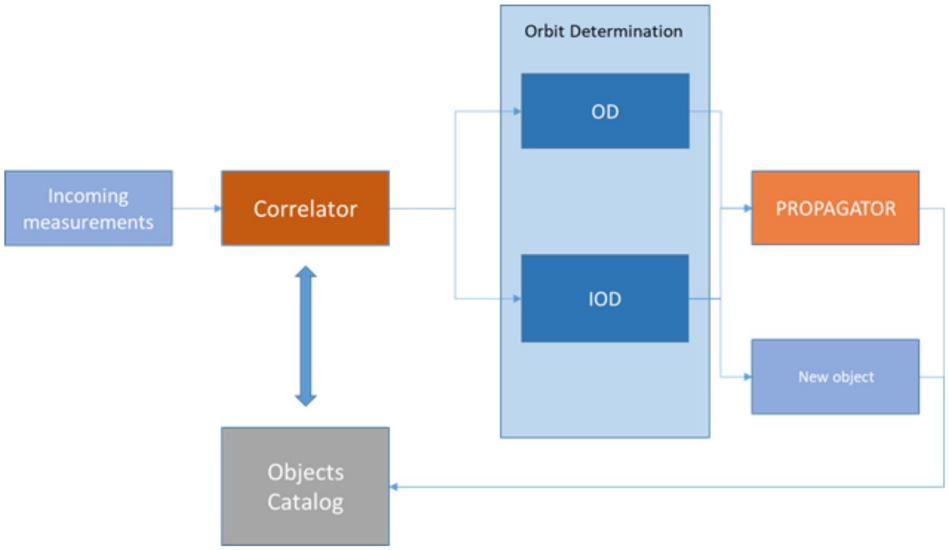

Figure 1.2: Catalogue maintenance: correlation and OD flow. Image source: [11].

Initially the sensor network provides the measurements of the observed objects. These are then processed in different ways, according to whether or not the orbit shall be determined and included for the first time in the catalog.
In the presence of a fragmentation event, the problem of early cataloging of generated objects shall be solved in order to limit cascade events potentially originated from a first break-up. Indeed, with accurate and quickly available estimated trajectories, Colli-

sion Avoidance Maneuvers (CAM) can be promptly planned. In [10] a cataloguing chain involving Track-to-Orbit (T2O) and Track-to-Track (T2T) approaches is proposed. In particular, the first is able to correlate a track (that is an ensemble of observations of a fragment) to an already catalogued orbit, subsequently updating its orbit through an Orbit Determination (OD) process. T2T allows instead to add to the catalog the tracks that have not been correlated to any existing fragment, by grouping those assumed originated by a common object [10]. Other approaches aimed at optimizing the catalogue maintenance process exploit alternative metrics: [12] demonstrates the use of a control-effort based distance metric to both correlate observed objects with catalogued ones and to detect and characterize planned maneuver, in presence of boundary conditions uncertainty. More established approaches, such as the one exploited in the Italian SST Operation Centre (ISOC) and reported in [11], leverage a statistical index based on the Mahalanobis Distance for the correlation process, and either batch or sequential filters for the orbit refinement.

1.3. Fragmentation events

As documented so far, it is clear that the timely monitoring of a on-orbit break-up as well as fast and accurate procedures to forecast the trajectories of resultant objects are of paramount importance. However, accomplishing this entails prior characterization of the event, to identify where and when the generated fragments propagate from the primary object.

Fragmentation events include generally explosions and collisions. In the first case, the object from which the fragments originate is defined as the parent, whereas in the second case the most massive body involved in the collision is called “target”, while the smallest "projectile” [13]. The most common wording labels the objects involved in a collision as primary and a secondary.

The detection of both epoch and location of a fragmentation event has been previously investigated in the context of this research topic, as it allows operationally to predict the evolution of fragments clouds. In [14] the event epoch is identified through a backward propagation of each fragment of the analysed cloud. At each time step the distance between the propagated state and the centre of mass of the cloud is computed, and the event is detected where this distance reaches a minimum. In [15] the breakup time is identified within an approach to correlate known fragments with possible parent objects. To achieve this, five distance metrics are applied (D-Criterias, Minimum Orbital Intersection Distance (MOID) and nodal distance) and investigated in terms of accuracy of the produced results. Despite the ease and effectiveness of this method, numerous ephemerides

of various fragments are assumed to be known and associable with an already catalogued parent object. This facilitates the epoch estimation, but it represents a less frequently applicable assumption in a realistic operational scenario. The assumption of availability of many TLEs is leveraged in [16] as well, where the tool PUZZLE is described. The latter estimates the epoch of a fragmentation event, both in the short and long-term scenarios, through a first pruning and filtering of non-relevant TLEs, and a subsequent analysis of the orbital elements of the remaining ones. Indeed, close to the breakup event, the generated fragments present similarities in some of the Keplerian elements. As stated above, the availability of accurate and numerous orbital states of fragments originated from the event is a "quite optimistic assumption" [17]. Instead, in the context of this work, it is assumed that the estimation of fragmentation epoch is required shortly after the event is alerted, when a small number of debris ephemerides (or a single one) is known. This fundamental premise comes from the FRagmentation Epoch Detector (FRED) algorithm, representing the starting point for the implementation of a new routine. FRED also aims to detect the epoch of a fragmentation event, starting from one ephemeris of the parent object and a single orbital state of a generated fragment. In particular, the approach is stochastic: different distance metrics are investigated to compare the statistical distributions of MOID and relative distances between parent and fragment. Fragmentation epoch candidates are first identified and then ranked according to the statistical distance between the two distributions. The best fragmentation epoch is finally returned in terms of mean value and standard deviation [17].

1.4. Scope and structure of the thesis

As mentioned, a prompt cataloging of the observed fragments is necessary to prevent future consecutive break-ups or minimize them. However, the detection of a fragment and the determination of its orbital state may be improved through additional information regarding its origin, specifically its location and epoch. This data is crucial for predicting its dispersion and ensuring precise orbit maintenance in the catalog. It allows for the planning of appropriate further observations aimed at preventing potential future collisions. A comprehensive characterization of the event also entails the ability to associate the observed fragments with a parent object.
Therefore this work aims to address the following research questions:

- Can Conjunction Analysis (CA) techniques be leveraged for the accurate detection of a fragmentation event epoch?
- Can CA techniques provide criteria to associate a detected object with the primary

one?

- Can the approach implemented in FRED be enhanced with alternative metrics, such as Probability of Collision (PoC), for the characterization of fragmentation events?

The last question arises seeing that the following research is conducted starting from the work carried out in [17].
The work conducted to address the previous questions is described in the following chapters. In particular, Chapter 2 provides an overview of fundamental concepts and techniques of astrodynamics, such as orbital state propagation and uncertainties. Moreover, a comprehensive review of fragmentation analysis, encompassing mathematical models of the break-up scenarios and PoC computation methods, is included. Finally, a section is devoted to the research conducted in [17], briefly describing the approach developed in FRED and mentioning potential modifications proposed in this thesis. Chapter 3 provides a step-by-step and detailed description of the routine implementation. It includes the definition of the required inputs and it outlines codes used for estimating the fragmentation epoch and associating the fragment with the parent object. In Chapter 4, the results of numerical simulations conducted on the test case are discussed. The routine performance are critically analysed and compared to FRED case. Conclusions and potential future developments of this work are finally depicted in Chapter 5.

2 | Fundamentals

Some of the most significant mathematical tools exploited in this work are summarized in this chapter. In Section 2.1 the models for orbital state propagation applied in the conducted simulations are briefly described. In Section 2.2, the employed statistical representation and Uncertainty Propagation (UP), based on Gaussian Mixture Models (GMM), is presented. Section 2.3 is dedicated to a brief mention of the model used for simulating the break-up and deriving of the fragments cloud data. In Section 2.4, an overview of the current theory and methods for collision risk assessment in the short-term scenario are described, together with the problems related to the PoC evaluation. Finally, 2.5 describes briefly FRED routine and mentions the modified aspects in the newly developed algorithm.
The standard reference frame used in this work is the Earth-Centered Inertial (ECI) frame. Except for the computation of the PoC, where state and covariance are converted to the encounter frame, or if specified otherwise, position and velocities are always reported in ECI. The leveraged time reference systems are the J2000 Ephemeris Time (ET) ([18]) and the Coordinate Universal Time (UTC).

2.1. Propagation models

There exist several models for propagating the orbital state, and below are briefly summarized those applied in the developed routine.
The first and simplest approach involves solving the two-body problem (Equation 2.1), resulting in what is referred to as Keplerian model.

$$\ddot{\boldsymbol{r}} = -\mu \frac{\boldsymbol{r}}{|\boldsymbol{r}|^3} \tag{2.1}$$

In absence of perturbations, the orbital elements between different time instants on the orbit remain constant, except for the true anomaly. Knowing the conversion between anomalies and mean motion solved with Kepler's equation, the individual anomalies can be simply updated and then position and velocity vectors as well. This approach does

not involve a numerical propagation, hence it results to be the most efficient one among the different models. However it is also the less complete and realistic, due to strong perturbations present in the Near-Earth environment which are neglected.
When additional accelerations besides that of the primary body are involved, the problem is modified as follows:

$$\ddot{\boldsymbol{r}} = -\mu \frac{\boldsymbol{r}}{|\boldsymbol{r}|^3} + \boldsymbol{a}_p \tag{2.2}$$

with $\boldsymbol{a}_p$ including any perturbations to be considered.
One of the most common analytical models, that is also applied in this thesis, is the Simplified General Perturbations model 4 (SGP4). It accounts for different perturbations (secular and periodic variations due to Earth oblateness, luni-solar gravitational effects, gravitational resonance effects, orbital decay due to drag [17]), still retaining the computational speed of an analytic method. However, SGP4-based propagators include the use of True Equator Mean Equinox (TEME) reference frame, and the conversion from ECI to TEME, implemented in this work through a fixed-point iteration process, limits its accuracy.

2.2. Uncertainty Propagation

The prevailing approach to depict orbital uncertainty involves approximating the initial distribution through a Gaussian representation. Subsequently, linearized model based on the use of the State Transition Matrix can be employed to advance the mean and covariance of the initial state over time. However, this method can introduce substantial inaccuracies when predicting uncertain orbits over extended durations and high levels of dynamical non-linearity. In response to these issues, the most basic methods rely on Monte Carlo propagations. These however demand large computational effort, becoming prohibitive in the case of high-dimensional problems.

2.2.1. Unscented Transform

The Unscented Transform (UT) method ([19]) solves the issues described above, combining nonlinear functions for propagation with acceptable computational costs. It exploits a set of samples, called sigma points $\boldsymbol{\chi}$, generated as:

$$\begin{cases} \boldsymbol{\chi}_0 = \boldsymbol{x} \\ \boldsymbol{\chi}_i = \boldsymbol{x} + \Delta\boldsymbol{x}_i \quad \text{for } i = 1, ..., N \end{cases} \quad \text{with} \quad \begin{cases} \Delta\boldsymbol{x}_i = (\sqrt{c\boldsymbol{P}_x})_i \quad \text{for } i = 1, ..., N \\ \Delta\boldsymbol{x}_{i+N} = -(\sqrt{c\boldsymbol{P}_x})_i \quad \text{for } i = 1, ..., N \end{cases}$$

The vector $\boldsymbol{x}$ corresponds to the mean state of the initial Gaussian distribution to propagate in time, while $\boldsymbol{P}_x$ represents its covariance matrix (in position and velocity). The sigma points are then propagated through a nonlinear dynamics function (obtaining $\boldsymbol{\mathcal{Y}}_i$), and the sample mean and covariance are computed. Generally, a weighted approach can be applied:

$$\hat{\mathbf{y}} = \sum_{i=0}^{2N} W_i^{(m)} \boldsymbol{\mathcal{Y}}_i \qquad\qquad \boldsymbol{P}_y = \sum_{i=0}^{2N} W_i^{(c)} (\boldsymbol{\mathcal{Y}}_i - \hat{\mathbf{y}})(\boldsymbol{\mathcal{Y}}_i - \hat{\mathbf{y}})^{\mathrm{T}}$$

where N = 6 and the weights are generated through a set of parameters with standard values $\alpha = 1e-3$, $\beta = 2$, $k = 0$ and $c = \alpha^2(N+k)$:

$$\begin{cases} W_0^{(m)} = 1 - \dfrac{N}{\alpha^2(N+k)} \\ W_i^{(m)} = \dfrac{1}{2\alpha^2(N+k)} \qquad \text{for } \ i = 1, ..., 2N \end{cases} \qquad \begin{cases} W_0^{(c)} = (2 - \alpha^2 + \beta) - \dfrac{N}{\alpha^2(N+k)} \\ W_i^{(c)} = \dfrac{1}{2\alpha^2(N+k)} \qquad \text{for } \ i = 1, ..., 2N \end{cases}$$

2.2.2. Gaussian Mixture Models

The UP approach applied in this thesis is comprised of the GMM, which represent a valuable compromise between the Gaussian approximation and the computational demand of Monte Carlo techniques. Its underlying concept is to approximate any Probability Density Function (PDF) through a weighted sum of N Gaussian PDFs with smaller covariances:

$$p(\boldsymbol{x}) \approx \sum_{i=1}^{N} \alpha_i p_g(\boldsymbol{x}; \boldsymbol{\mu}_i, \boldsymbol{P}_i) \qquad\qquad \sum_{i=1}^{N} \alpha_i = 1$$

Therefore, an initial Gaussian distribution can be discretized as well with a number of smaller Gaussians [20].

The weight, means and covariance matrices of the i-th element are derived through available univariate splitting libraries, applied to the multivariate distribution related to the orbital state. Specifically, the splitting is performed along a single direction, which is usually chosen as the direction of largest nonlinearity or highest uncertainty. Once generated, each element of the GMM can be propagated through one of the existing UP methods. For instance, in this work the splitting is applied on the initial Gaussian distribution and the UT is then employed on each Gaussian sub-component to propagate mean states and covariance matrices to a desired set of epochs.

As previously mentioned, splitting the initial distribution into a GMM results in a decreased covariance size for each newly created element. This reduction of the approxima-

tion domain enables to capture the shape of the final non-Gaussian distribution far more precisely than with the propagation of the initial Gaussian ([21]). Given these benefits, this approach is explored and employed in the implementation.

2.3. NASA Standard Breakup Model

The novel routine implemented in this work requires in input a data set of simulated fragments, including specifically their mean state and covariance. For this reason, the first step involves modelling the fragmentation event and generating a certain number of objects from which fictitious measurements are derived. The NASA Standard Breakup Model (SBM) [22] has been developed over the years based on data acquired from orbital explosion and collision events, with the aim of predicting essential information about the distribution of generated debris. Specifically, it enables the determination of their quantity, size, area-to-mass ratio, and ejection velocity.
For the purpose of this work, the SBM allows to compute the orbital states of the fragments derived from the parent object involved in the tested scenario. The position vector of each debris is exactly the same as the parent one at the epoch of the event. Instead, the fragment velocity vector is obtained by adding a set of impulses to the parent velocities, depending on the type of event (collision or explosion) and the ejection velocity distribution.

$$\begin{cases} \boldsymbol{r}^f = \boldsymbol{r}^p \\ \boldsymbol{v}^f = \boldsymbol{v}^p + \Delta\boldsymbol{v}_{SBM} \end{cases} \qquad \text{at } t_{event} \tag{2.3}$$

Additionally, the SBM is applied in the thesis to derive the number of fragments produced by the simulated event, as well as the size or characteristic length of each fragment.

2.4. Conjunction Analysis

As mentioned in Chapter 1, CA refers to the assessment of possible in-orbit collisions between any object. When two objects are dangerously close to each other, quantities such as miss-distance and collision probability shall be computed. If the distance value falls below a certain threshold, or the PoC is sufficiently high, the collision risk cannot be neglected. If this is the case then a series of operations (such as CAMs) can be performed in a timely manner. The computation of the PoC is usually performed at the Time of Closest Approach (TCA), corresponding to the epoch of closest approach distance

between primary and secondary object in the encounter reference frame. The latter can be centered in the primary object. It has the positive z axis along the relative velocity vector, the positive x axis pointing to the secondary object and belonging to the B-plane, and the y axis completing the right-handed system. The combined Hard-Body Radius (HBR) is obtained by summing the respective hard-body radii of the two space objects, assumed in this context as spherical. This radius also corresponds to the radius of the combined sphere, which can be centered on the secondary object (Figure 2.1).

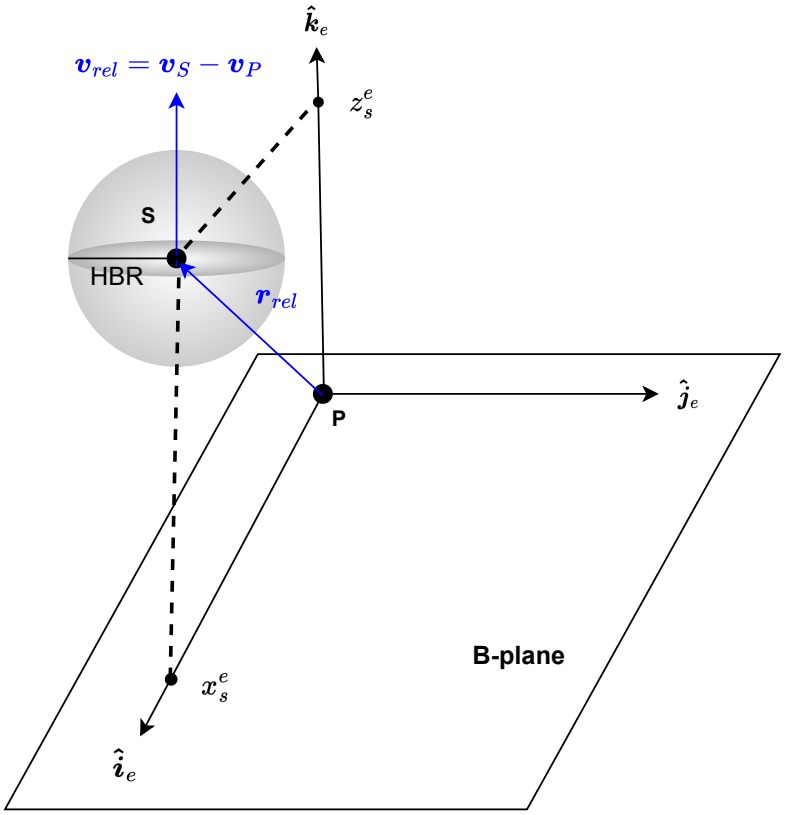

Figure 2.1: Primary and secondary objects in the encounter frame.

Conjunctions events are commonly classified in two categories: long-term and short-term encounters. The short-term encounters involve high relative velocities in the order of several kilometers per second, with elapsed time in the encounter region being "a fraction of a second or at most a few seconds" [23]. From this premise, a series of assumptions arise and simplify the calculation:

- The relative motion between two objects is uniform and rectilinear;
- The velocity uncertainty of the two objects can be neglected because assumed too small compared to the relative velocity;

- The uncertainties on the position are assumed Gaussian, non-correlated for the two objects and constant during the encounter.

Finally, assumptions of perfectly spherical shapes of the RSOs and single collision during the encounter are also included, to further simplify the computation.
When the relative velocity between the involved objects is not sufficiently high, and the previous assumptions are not valid, methods designed for the long-term encounters shall be applied. These are typically more complex and less used in the context of LEO regime, where satellites orbit at high speed. Therefore in this thesis as well the former assumptions are considered valid and only short-encounter PoC methods are summarized and leveraged in the implementation.

2.4.1. PoC computation methods

Various methods exist in the current literature for the short-term computation of the PoC. Those investigated in this thesis and implemented in the routine are briefly described below. All are based on the assumptions described in Section 2.4, which allow to simplify the computation. The basic concept is common to all methods: if the primary RSO with its uncertainty ellipsoid passes within the combined sphere, then there is a collision whose PoC is defined as the probability of this to occur ([23]). To compute this probability over the encounter period, the integral of the combined PDF shall be performed over the integration volume, which in the case of short-term assumptions is a tube produced by the motion of the sphere encountering the *joint covariance ellipsoid* ([23]) centered on the primary RSO (Figure 2.2a).

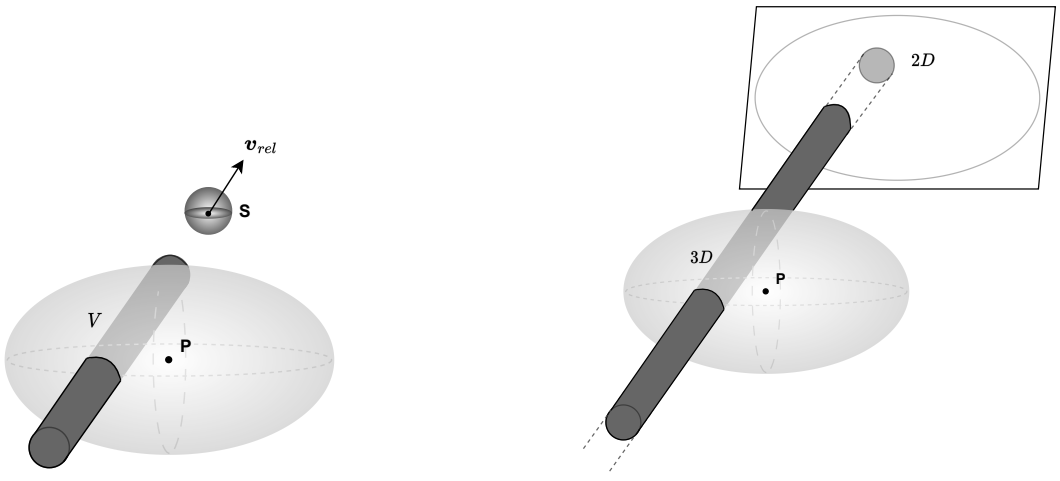

(a) 3D integration domain

(b) 2D integration domain

Figure 2.2: Integration domains during short-term encounters.

This results in the following triple integral:

$$P^c = \iiint_V p_g(\boldsymbol{x}_{TCA}; \boldsymbol{\mu}_{rel}, \boldsymbol{P}_C)\, dV$$

with the PDF assumed constant in time. The PDF is here taken at TCA, $\boldsymbol{\mu}_{rel} = \boldsymbol{\mu}_S - \boldsymbol{\mu}_P$ denotes the mean relative position between the two objects and $\boldsymbol{P}_C = \boldsymbol{P}_P + \boldsymbol{P}_S$ is the combined covariance matrix of the relative position, retrieved as a simple sum of the two covariance matrices owing to the assumptions of non-correlated position uncertainties. A further simplification is made in the all described approaches: the integration tube is assumed infinite. As shown in Figure 2.2b, this allows to reduce the integration domain to the disk projection of the combined sphere onto the encounter plane and having radius equal to the HBR. The collision probability can be thus written as a 2D integral along the relative velocity direction (following the notation in [24]):

$$P^c = \frac{1}{2\pi\sqrt{\det(\boldsymbol{P}^e_{xy})}} \int_A \exp\left(-\frac{1}{2}(\mathbf{r} - \boldsymbol{\mu}^e_{xy})^T (\boldsymbol{P}^e_{xy})^{-1} (\mathbf{r} - \boldsymbol{\mu}^e_{xy})\right) d\mathbf{r}$$

where the covariance matrix $\boldsymbol{P}^e_{xy}$ can be written as:

$$\boldsymbol{P}^e_{xy} = \begin{bmatrix} (\sigma^e_x)^2 & \rho^e_{xy}\sigma^e_x\sigma^e_y \\ \rho^e_{xy}\sigma^e_x\sigma^e_y & (\sigma^e_y)^2 \end{bmatrix}$$

with $\sigma^e_x > 0$ and $\sigma^e_y > 0$ standard deviations of the relative positions along $\hat{\boldsymbol{i}}_e$ and $\hat{\boldsymbol{j}}_e$ and $\rho^e_{xy} \in (-1, 1)$ the correlation coefficient ([25]). The integration subscript A refers to the area of the circle projected on the encounter plane, $\boldsymbol{\mu}^e_{xy} = (x^e_s, 0)$ corresponds to the first coordinate of the relative position vector and $\mathbf{r}$ is the integration variable representing the rectilinear relative motion. Furthermore, the cross term of the Gaussian function can be discarded with a rotation from the encounter frame to the principal axes of the covariance matrix, achieving $(x^e, y^e) \rightarrow (x^u, y^u)$. This transformation is such that the new coordinates (x^u, y^u) are along the major and minor axis and their standard deviations (σ^u_x, σ^u_y), if squared, correspond to the maximum and minimum eigenvalues of $\boldsymbol{P}^e_{xy}$. This transformation (better detailed in [26]) reduces the PoC computation to this final integral:

$$P^c = \frac{1}{2\pi\sigma^u_x\sigma^u_y} \int_A \exp\left(-\frac{1}{2}\left(\frac{(x^u - x^e_s)^2}{(\sigma^u_x)^2} + \frac{(y^u - y^e_s)^2}{(\sigma^u_y)^2}\right)\right) dx\, dy$$

At this point, the evaluation of the 2D integral branches out into several approaches. Chan's approach in [27] is based on an analytical formula. To compute the PoC, the

integral of an isotropic bivariate Gaussian PDF ($\sigma_x = \sigma_y$) in the encounter plane is considered ([23]). The integration domain is still a circle centered in the encounter plane origin. To reduce the integral to a single variable, the Rician formulation is used together with a Bessel function included in the integrand. Hence, an expression of infinite series is found for the analytical formulation of the PoC. It is highlighted in literature that Chan's method is highly computationally efficient, however the isotropic approximation may introduce numerical truncation errors in some cases. In [28] Serra reports an analytic formulation similar to Chan's, though derived with no simplifying assumption. The formula has the shape of a "convergent power series whose coefficients verify a linear recurrence" ([28]). It is retrieved leveraging Laplace transform and the properties of D-finite functions. The numerical simulations performed by the authors demonstrate the high accuracy and speed of this approach. Garcìa Pelayo's approach ([29]) is based on an analytical expansion involving Hermite polynomials, through which the PDF integral, resulting in the PoC value, can be computed. Lastly, Bai's analytical method ([30]) can be mentioned; it employs the integral of the PDF, converted from anisotropic to isotropic, within an ellipsoid approximated then to a circular region. Once simplified, the integral is expressed through an infinite series. For this reason Bai's method appears quite similar to Chan's one; however, from test simulations conducted in [23], Bai's formulation results to be more efficient and accurate.

Regarding numerical methods, Alfano's one has been specifically implemented following the formulation in [31] for this thesis, and validated through the test cases in [32]. This method should be more computationally efficient than other existent numerical methods, however less fast of course than the analytical formulations. To compute the 2D integral, Alfano derived a series including error functions and exponential. This then breaks down into m-even and m-odd components and finally the PoC is computed through them using the Simpson's one third rule. An expression to determine the order m of the series allowing to obtain the best accuracy on P^c is also reported in [32]. Foster and Estes derived a collision probability model (in [33]) exploiting polar coordinates in the encounter plane. It "exhibits good performance" (according to [23]), however the efficiency of this method depends on the step size adopted for the polar variables. In [34], Patera proposes a method which is still numerical, however able to reduce the computational time. It exploits a loop integral of the symmetric PDF along an ellipse (derived through a conversion from the combined circle). Patera's method, besides being significantly faster than other numerical approaches, is also applicable to RSOs which are not assumed spherical.

In Appendix A, are reported exclusively the algorithms of those approaches which can be applied in the routine, namely Chan's, Alfano's and Serra's (also called LAAS method).

2.4.2. PoC dilution problem

It is deemed important to briefly address an aspect that should not be overlooked in the context of collision probability calculation following the orbital propagation of uncertainties. This problem, referred to as PoC dilution and investigated by Alfano in [35], may arise when the positional uncertainty is very high. In this case the use of Gaussian probability-based computations yields a very low PoC value, which might lead to a missed alert of possible conjunction. The effects of dilution are clearly illustrated in Figure 2.3.

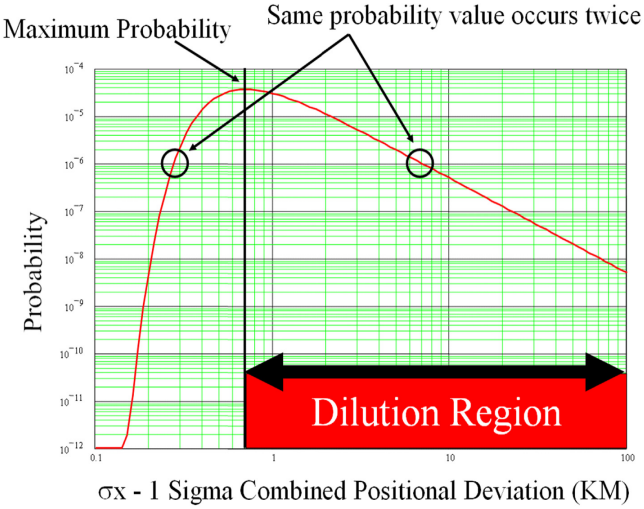

Figure 2.3: Dilution curve and dilution region. Image source: [36]

.

Figure 2.3 reports the impact of position covariance variations on the PoC value, proving a typical relationship between collision probability and covariance size for fixed miss distance and constant combined HBR. The boundary of the dilution region is defined by the scaled, combined covariance that yields the maximum probability. On the left side of this boundary reduced positional uncertainty leads to a decreased collision probability. On the right side of the boundary, increased positional uncertainty also results in a decreased collision probability. Indeed, a substantial uncertainty implies limited confidence in the predicted miss distance, resulting in a low probability. This can be misleading, suggesting that satellite safety improves as data quality deteriorates.
Despite prior research efforts, including uncertainty scaling factors and Maximum Probability formulations [35], this thesis still employs the conventional computation methods above reported. However, an attempt has been made to mitigate the dilution problem by using low initial covariances, leveraging refined determination algorithms to prevent uncertainty explosion due to propagation over time.

2.5. FRED algorithm

This research is partly motivated by the need to assess if the performance of FRED algorithm ([17]) can be anyway improved, by applying new evaluation metrics originating from CA techniques, to determine the epoch of a fragmentation event. FRED algorithm deals with the problem of epoch identification dropping the assumptions that an ensemble of orbital states is available for the fragments cloud. Instead, only one is available in input, together with the parent state in the form of a single TLE. This approach was chosen to simulate an operational scenario where the observation is requested shortly after the event alert, implying that a low number of fragments ephemerides is accessible. Indeed, prompt identification of the event epoch allows to schedule new measurements to better predict the fragments cloud evolution, monitor the debris proliferation they may cause, and possibly refine the fragmentation characterization.

An important aspect of FRED method is the application of a stochastic approach. In a very concise manner, the tool obtains possible fragmentation epochs, from the numerous samples generated, and then it ranks them according to their statistical similarity between the relative distance distribution and the MOID distribution. To keep the writing concise, the approach is not explained in details here, but the algorithm flowchart is provided in Figure 2.4. For sake of clarity, T^p is the parent orbital period, used to sample the analysis window and obtain the t_i starting epochs of each periodicity. The j-th samples are generated from the single fragment state through a multivariate normal distribution.

As explained in the next chapter, the initial part of the routine implemented for this work draws inspiration from the MOID transit computation performed in FRED. In a very similar way, a set of candidates epochs is thus retrieved. However, the Monte Carlo with samples generation is replaced by a statistical representation based on GMM for both the parent object and the fragment. Furthermore, the metric applied to rank the candidate epochs in FRED is replaced with the use of collision probability. The latter is exploited to serve as a criterion for converging to an estimated epoch.

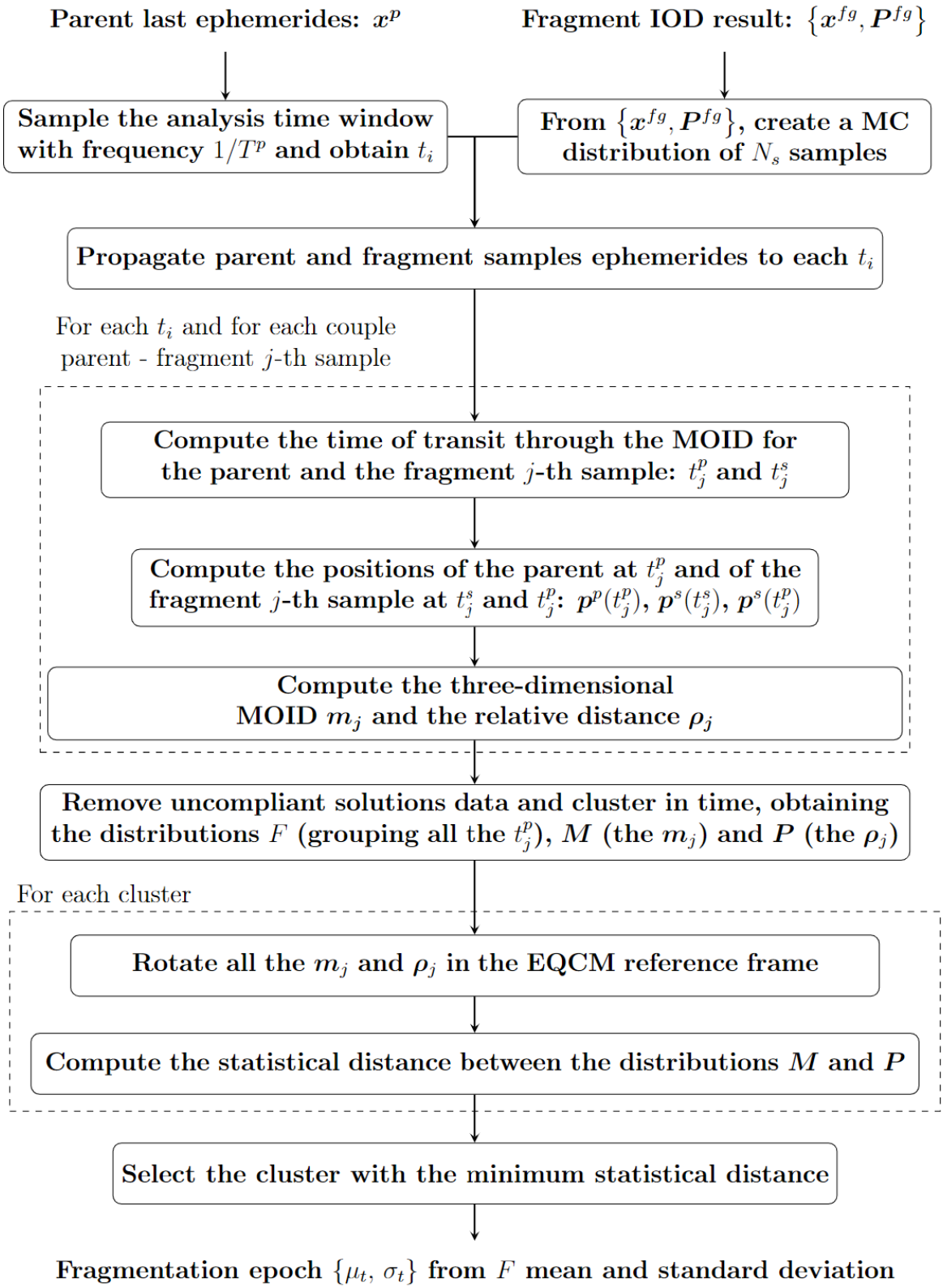

Figure 2.4: FRED flowchart. Source: [17]

.

3 | Algorithm implementation

In the following sections, the components of the flow that makes up the implemented routine are described in detail. For an overview, refer to Figure 3.1. Briefly, the described approach consists of the following series of steps. A set of candidate fragmentation epochs is obtained by computing the epochs of the parent passage through the MOID, for all combinations of the mean states elements of parent and fragment distributions retrieved by the application of GMM. These epochs are considered candidate TCAs and are then refined. Hence, the collision probability criterion is introduced to identify the periodicity at which the fragmentation is most likely to have occurred. Finally, an additional metric (Mahalanobis Distance) is used to identify the combination of parent and fragment elements that are statistically closest. This is done to ultimately determine a single estimated fragmentation epoch corresponding to the periodicity and parent-fragment elements selected by the statistical criteria.

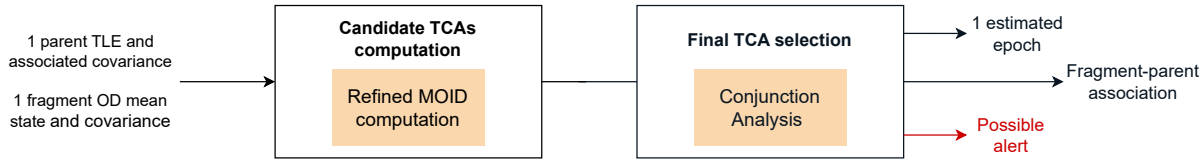

Figure 3.1: Routine flow chart.

Section 3.1 describes a preliminary step to the routine aimed at generating a covariance matrix for the parent object. Section 3.2 illustrates the splitting approach applied for the GMM generation. Section 3.3.1 and Section 3.3.2 describe in detail the algorithm, respectively its first and second portion. In Section 3.4 the reliability criteria aimed to produce an alert on the correctness of the solution is reported. Finally in Section 3.5 the analysis intended to verify the association of the fragment object to the event is presented.

3.1. Parent covariance association

Crucial inputs of the algorithm are the mean states of the parent and the fragment objects, with their associated Gaussian covariance matrices. For the fragment, the data set

generation (Section 4.2) is leveraged, through simulated observations and subsequent OD processes. However, for the parent object, it is necessary to associate somehow a covariance matrix, that represents the uncertainty of the state obtained from the available TLE (which is a deterministic information). To do so, the method of covariance association proposed in [1] was first investigated, however discarded due to its inadequacy, which showed up in the result of the UP through GMM. In [1], the TLE accuracy is assessed through the generation of pseudo-observations, a subsequent OD algorithm and the final statistical computation of residuals between the states derived from the TLE data and the pseudo-states. The standard deviations of these residuals are the estimated TLE uncertainties, then inserted into look-up tables. The problem for which this approach was discarded is that the estimation of uncertainties is proposed and validated solely for the three position components (in different reference frames). Regarding the velocity components, a different approach could imply the use of a fictitious and diagonal sub-covariance, however this was discovered to be not realistic and accurate. This is evident from the misleading representation of the GMM after propagation over time, obtained by the test case on the TLE of object Cosmos 1408 and reported in Section 4.3.
To solve the issue, a different approach for the whole covariance association was sought and subsequently found in [2]. A covariance matrix and an auto-correlation function are both obtained by the author exploiting solely a set of publicly available TLEs in a time span of two weeks maximum. The approach to estimate the covariance matrix $\boldsymbol{P}_{tle}$ at the epoch t_{tle} is here summarized:

1. The epoch of interest t_{tle} is referred to as primary epoch.
2. N_{tle} secondary TLEs are downloaded from Space-Track website [37], up to an arbitrary number of days before t_{tle} epoch (within two weeks before).
3. Each of the secondary TLEs states is propagated forward in time (with SGP4) up to t_{tle}.
4. For each secondary TLE, the residual at t_{tle} is computed ($\boldsymbol{x}$ denotes the state vector of position and velocity):
$$\delta\boldsymbol{x} = \boldsymbol{x}'' - \boldsymbol{x}'$$
between secondary ($\boldsymbol{x}''$) and primary ($\boldsymbol{x}'$) states.
5. The mean of the obtained N_{tle} residuals is computed, and here called $\boldsymbol{\mu}_{\delta\boldsymbol{x}}$.
6. The covariance is generated through the sample covariance definition:
$$\boldsymbol{P}_{tle} = \frac{\sum_{i=1}^{N_{tle}} (\delta\boldsymbol{x}_i - \boldsymbol{\mu}_{\delta\boldsymbol{x}})(\delta\boldsymbol{x}_i - \boldsymbol{\mu}_{\delta\boldsymbol{x}})^T}{N_{tle}}$$

In the case of this work a number of $N_{tle} = 5$ was downloaded and used.
The approach just described was applied to the parent state extrapolated from the input TLE of the specific test case. The numeric result of the covariance generation is reported in Section 4.3, and the corresponding GMM distribution is represented after propagation in time (Figure 4.4b), showing the benefits of the new shape of the parent covariance matrix.

3.2. GMMs generation

The uncertainty representation and propagation through GMM is used in this work due to the benefits described in Section 2.2.2.
Specifically, the splitting direction along which the univariate library is applied is derived in the following way:

1. The covariance matrix belonging to the distribution to split is made dimensionless, first in position and then in velocity, by dividing its elements by the trace of the positional and velocity diagonals, respectively.
2. The eigenvalues of the dimensionless covariance matrix are computed.
3. The highest of the eigenvalues is identified, and with it the corresponding eigenvector of the initial covariance matrix.
4. The derived eigenvector represents the selected splitting direction, therefore it becomes the input to the splitting library.

In practice, this translates to exploiting the direction of maximum uncertainty. In addition, the adimensionalization enables equal consideration of the uncertainties related to the position and to the velocity components, when selecting the splitting direction.
The steps reported above for the splitting process are applied on both parent and fragment Gaussian distributions at initial epoch. Thus, the obtained mean states and covariance matrices are propagated over time exploiting the UT, due to its accuracy in capturing non-linearities, besides the computational simplicity and speed.

3.3. Fragmentation epoch estimation

3.3.1. Candidate TCAs computation

The first block in the algorithm (Figure 3.2) computes a set of candidate epochs of possible encounters for each element i_p of the parent mixture ($\{\boldsymbol{x}_{i_p}^p, \boldsymbol{P}_{i_p}^p\}$) and for each element i_f

of the fragment mixture ($\{\boldsymbol{x}_{i_f}^f, \boldsymbol{P}_{i_f}^f\}$).

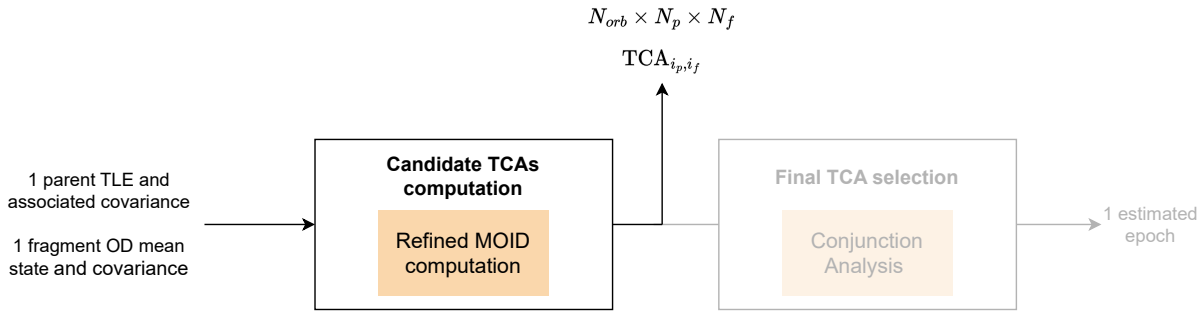

Figure 3.2: Routine flow chart. First block highlighted.

The applied approach is very similar to what is done in FRED, with the difference being that Monte Carlo samples are replaced by the N_p elements from the parent mixture and N_f elements from the fragment mixture, resulting in $N_p \times N_f$ candidate fragmentation epochs as output. Specifically, these are obtained as the epoch of passage through the MOID location for the parent, whose ephemeris is deemed to be more reliable than the fragment state, output of an OD process. This epoch is obtained through an analytical computation of the MOID and is subsequently refined through the iterative process presented in [17]. The ephemeris of the original RSO involved in the fragmentation is referred to as $\boldsymbol{x}^p$ and is dated to t_{tle}, epoch of the last TLE available before the event. The covariance matrix of the parent $\boldsymbol{P}^p$ is also dated to t_{tle} and associated to $\boldsymbol{x}^p$ according to the procedure described in Section 3.1. The event is considered to have occurred at $t_0 > t_{tle}$ and the related alert has been notified at $t_a > t_0$. Some hours later, a fragment is detected by a surveillance radar at $t_{od} > t_0$ and its mean orbital state $\boldsymbol{x}^f$ and covariance matrix $\boldsymbol{P}^f$ are computed from an OD process [17].
The first portion of the routine is reported in Algorithm 3.1 and is structured as follows:

1. The time window $[t_{tle}, t_a]$ is sampled with frequency $1/T_p$, where T_p is the parent orbital period computed from the input TLE. This results in N_{orb} number of epochs t_i, each related to the i-th periodicity.

2. In order to include the state uncertainty in the event epoch identification, N_p Gaussian Mixture Elements (GMEs) and N_f GMEs are generated through the splitting approach described in Section 3.2. In particular, the state vectors $\boldsymbol{x}_{i_p}^p$ with $i_p = 1, ..., N_p$ and $\boldsymbol{x}_{i_f}^f$ with $i_f = 1, ..., N_f$ are produced.

3. A nested loop is started for each parent GME and fragment GME.

4. The states of parent and fragment elements are propagated to each t_i.

5. For each t_i, the MOID distance and the epochs of transit through the MOID of both parent element i_p and fragment element i_f are computed analytically, according to [38] and leveraging the Kepler's equation. The results are indicated as $t^p_{i_p,i_f}$ and $t^f_{i_p,i_f}$. The parent i_p and the fragment i_f state vectors are propagated up to $t^p_{i_p,i_f}$ and $t^f_{i_p,i_f}$ respectively, resulting in the orbital states $\boldsymbol{x}^p_{i_p}(t^p_{i_p,i_f})$ and $\boldsymbol{x}^f_{i_f}(t^f_{i_p,i_f})$, and the analytical computations of $t^p_{i_p,i_f}$ and $t^f_{i_p,i_f}$ are updated. Both epochs are iteratively modified in this manner until, between two consecutive steps, they do not change anymore (according to a tolerance set equal to $1e-03$ s) ([17]). It is important to specify that this iterative cycle is performed to include the perturbations that are instead not considered in Gronchi's formulation ([38]), which relies on a purely analytical model. By propagating at each iteration the GMEs mean states up to the passage epochs through the MOID, and updating then again its value through Gronchi's approach, the perturbations of the model (if any) are included. The iterative process results in $N_{orb} \times N_p \times N_f$ couples of $\left(t^p_{i_p,i_f}, t^f_{i_p,i_f}\right)$ and $\left(\boldsymbol{x}^p_{i_p}(t^p_{i_p,i_f}), \boldsymbol{x}^f_{i_f}(t^f_{i_p,i_f})\right)$.

6. The fragment i_f state vector $\boldsymbol{x}^f_{i_f}(t^f_{i_p,i_f})$ is propagated up to the epoch of transit of the parent element i_p through the MOID, resulting in $\boldsymbol{x}^f_{i_f}(t^p_{i_p,i_f})$. This is selected instead of the time of the fragment element i_f transiting through the MOID due to the higher reliability associated to the parent ephemeris.

7. To exclude unfeasible solutions, the $N_{orb} \times N_p \times N_f$ couples enter a filtering phase, applied on the epoch of parent element i_p transiting through the MOID ($t^p_{i_p,i_f}$). The first filter requires that the couples with combinations (i_p, i_f) for which $t^p_{i_p,i_f}$ is not included in the boundaries of the time window $[t_{tle}, t_a]$ are eliminated. With the second filter, for each t_i, the couples with combinations (i_p, i_f) for which $t^p_{i_p,i_f} < (t_i - T_p/2)$ or $t^p_{i_p,i_f} > (t_i + T_p/2)$ are filtered out. In this way, the passage epochs that, despite being calculated at the i-th periodicity, fall beyond t_i plus or minus a semi-period, are eliminated. The last filter is based on a Density-Based Spatial Clustering of Applications with Noise (DBSCAN) ([39]), applied to eliminate couples with combinations (i_p, i_f) which are considered outliers (setting the maximum time deviation to 5 minutes).

8. If $t^p_{i_p,i_f}$ related to all combinations (i_p, i_f) is not compliant for all N_{orb} periodicities, the fragment under analysis must be discarded. Therefore, it is accepted that in some scenarios not all fragments obtained from the data set and analysed return a result, as they are deleted after the application of the filters.

For the analysed fragment, if not discarded, the epochs of parent element i_p transiting

through the MOID ($t^p_{i_p,i_f}$) are then refined, exploiting the orthogonality between the relative position and the relative velocity. Specifically, the candidate TCAs are computed as the epochs where the scalar product between position and velocity is null, through an optimization function and applying the Keplerian model. The sequence of steps to compute the TCA between the state vectors of two generic primary and secondary objects ($\boldsymbol{x}_1$ and $\boldsymbol{x}_2$) given a first guess TCA_0 is the following:

1. The orbital elements of the primary object are computed from $\boldsymbol{x}_1$.
2. The orbital elements of the secondary object are computed from $\boldsymbol{x}_2$.
3. An iterative loop is started.
4. The orbital elements of both primary and secondary objects are analytically propagated, from TCA_0 to $\text{TCA}_0 + 10\text{s}$.
5. The Cartesian position and velocity vectors are determined at $\text{TCA}_0 + 10\text{s}$ for both objects (obtaining $(\boldsymbol{r}_1, \boldsymbol{v}_1)$, $(\boldsymbol{r}_2, \boldsymbol{v}_2)$).
6. The relative position ($\boldsymbol{r}_{rel} = \boldsymbol{r}_2 - \boldsymbol{r}_1$) and velocity ($\boldsymbol{v}_{rel} = \boldsymbol{v}_2 - \boldsymbol{v}_1$) are computed.
7. Equation 3.1 is solved in time through an optimization algorithm.

$$\boldsymbol{r}_{rel}(t) \cdot \boldsymbol{v}_{rel}(t) = 0 \tag{3.1}$$

8. The loop is continued until a maximum number of 1000 iterations is not reached.
9. The last epoch determined by the loop is considered close enough to the real TCA between the two objects.

In the particular case of the developed algorithm, the inputs to this refinement process are the TCA first guess ($t^p_{i_p,i_f}$) and the orbital states of each parent and fragment GME at that epoch ($\boldsymbol{x}^p_{i_p}(t^p_{i_p,i_f})$ and $\boldsymbol{x}^f_{i_f}(t^p_{i_p,i_f})$). This allows to obtain in output accurate candidate TCA epochs, in number $N_{orb} \times N_p \times N_f$ (one for each periodicity and for each combination parent-fragment GME). At this point each parent and fragment GME ($\{\boldsymbol{x}^p_{i_p}, \boldsymbol{P}^p_{i_p}\}$ and $\{\boldsymbol{x}^f_{i_f}, \boldsymbol{P}^f_{i_f}\}$) is propagated through an UT function to the refined TCAs, which represent the fragmentation candidate epochs.

3.3.2. Final TCA selection

The second block of the routine (Figure 3.3) aims to finally detect the fragmentation event epoch, given the parent-fragment couple under analysis. The inputs are obtained from

the first portion of the algorithm and are thus processed using typical metrics of CA and collision risk assessment.

Algorithm 3.1 Candidate TCAs computation

Inputs: $\boldsymbol{x}^p$, $\boldsymbol{x}^f$, $\boldsymbol{P}^p$, $\boldsymbol{P}^f$, $[t_{tle}, t_a]$, t_{od} N_p, N_f

$t_{window} = [t_{tle}, t_a]$ with step $T_p \rightarrow$ count N_{orb}
Generate N_p GMEs for the parent and N_f GME for the parent $\rightarrow$ obtain $\boldsymbol{x}^p_{i_p}$ and $\boldsymbol{x}^f_{i_f}$
for $i_p = 1 : N_p$ **do**
    Propagate $\boldsymbol{x}^p_{i_p}$ to each t_i
    for $i_f = 1 : N_f$ **do**
        Propagate backward $\boldsymbol{x}^f_{i_f}$ to each t_i
        for $i = 1 : N_{orb}$ **do**
            Compute MOID between $\boldsymbol{x}^p_{i_p}$ and $\boldsymbol{x}^f_{i_f}$
            Compute Time of Flight (TOF) to the MOID location through Kepler's equation
            Compute first guess for $t^p_{i_p,i_f}$ and $t^f_{i_p,i_f}$
            Set first guess for the states at $\boldsymbol{x}^p_{i_p}(t_i)$ and $\boldsymbol{x}^f_{i_f}(t_i)$
            while $t^p_{i_p,i_f}(k)$ - $t^p_{i_p,i_f}(k-1) > 1e-3$ or $t^f_{i_p,i_f}(k)$ - $t^f_{i_p,i_f}(k-1) > 1e-3$ and $k < 10$ **do**
                $k = k + 1$
                Propagate current $\boldsymbol{x}^p_{i_p}(t_i)$ to parent current TOF to MOID
                Propagate current $\boldsymbol{x}^f_{i_f}(t_i)$ to fragment current TOF to MOID
                Compute MOID between propagated states
                Update TOF to the MOID location through Kepler's equation
                Update $t^p_{i_p,i_f}$ and $t^f_{i_p,i_f}$
            end while
            Obtain final $t^p_{i_p,i_f}$ and $t^f_{i_p,i_f}$
            Compute final $\boldsymbol{x}^p_{i_p}(t^p_{i_p,i_f})$ and $\boldsymbol{x}^f_{i_f}(t^p_{i_p,i_f})$
        end for
    end for
end for
Apply filters on $t^p_{i_p,i_f}$
if $\forall\ i = 1 : N_{orb}$ && $(\forall\, i_p = 1 : N_p$ && $\forall\, i_f = 1 : N_f) \rightarrow t^p_{i_p,i_f} =$ NaN **then**
    Discard current fragment for the simulation
else
    for $i_p = 1 : N_p$ **do**
        for $i_f = 1 : N_f$ **do**
            for $i = 1 : N_{orb}$ **do**
                With $t^p_{i_p,i_f}$, $\boldsymbol{x}^p_{i_p}(t^p_{i_p,i_f})$, $\boldsymbol{x}^f_{i_f}(t^p_{i_p,i_f}) \rightarrow$ refine epochs
            end for
            Obtain N_{orb} TCA_{i_p,i_f}
            Propagate $\{\boldsymbol{x}^p_{i_p}, \boldsymbol{P}^p_{i_p}\}$ to each TCA_{i_p,i_f} with UT
            Propagate backward $\{\boldsymbol{x}^f_{i_f}, \boldsymbol{P}^f_{i_f}\}$ to each TCA_{i_p,i_f} with UT
        end for
    end for
end if

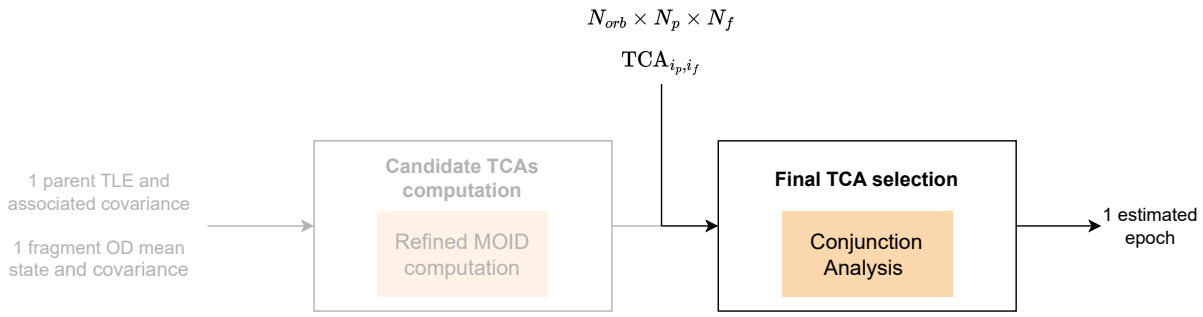

Figure 3.3: Routine flow chart. Second block highlighted.

Specifically, the event under analysis is treated as a conjunction between a primary object (the parent) and a secondary object (the fragment). This allows to assess the collision probability values at the periodicities in the analysis window, and determine where it is highest, providing an initial insight into the time interval where the encounter is most likely to have occurred. It is important to note that the MOID is a purely geometric parameter and depends on the orbits of the two objects. Being time independent, it does not provide information on the actual relative positions of the objects. Therefore, the CA allows to verify at which of the MOID passage epochs the encounter may truly occur.
The inputs required for this portion of the algorithm are the refined candidate TCA epochs at all periodicities and for all combination of GMM elements ($N_{orb} \times N_p \times N_f$ TCA_{i_p,i_f}). The mean states and covariance matrices of parent and fragment GMEs at these epochs are also required ($\{\boldsymbol{x}^p_{i_p}(\mathrm{TCA}_{i_p,i_f}), \boldsymbol{P}^p_{i_p}(\mathrm{TCA}_{i_p,i_f})\}$, $\{\boldsymbol{x}^f_{i_f}(\mathrm{TCA}_{i_p,i_f}), \boldsymbol{P}^f_{i_f}(\mathrm{TCA}_{i_p,i_f})\}$). This second portion of the routine is reported in Algorithm 3.2 and is structured as follows:

1. A nested loop is started for each parent GME and fragment GME.
2. For each t_i, the PoC between the current parent and fragment GMEs is computed, through one of the approaches reported in Section 2.4.1, selected by the user. If not, Chan's method is applied by default. The inputs entering the PoC computation algorithm are the distributions $\{\boldsymbol{x}^p_{i_p}(\mathrm{TCA}_{i_p,i_f}), \boldsymbol{P}^p_{i_p}(\mathrm{TCA}_{i_p,i_f})\}$, $\{\boldsymbol{x}^f_{i_f}(\mathrm{TCA}_{i_p,i_f}), \boldsymbol{P}^f_{i_f}(\mathrm{TCA}_{i_p,i_f})\}$ at the corresponding candidate TCA epochs. The covariance matrices are actually required solely in their positional components, as short-term approaches, which consider the velocity as a deterministic quantity, are employed. The HBR of the combined sphere is also required. The sphere radius can be selected for the parent object as its radar cross section, for instance, if this information is available. While, for the fragment, the sphere radius can be either derived from the characteristic length provided by the assumed break-up model, or assumed. Nevertheless, it is important to notice that, in the case of a fragmentation event analysis, any value employed for the HBR lacks of a physical meaning. Indeed, the combined

radius includes the contribute of the parent object dimensions, which however at fragmentation epoch does not exist physically. On the other hand this "paradox" does not occur in a classic collision risk assessment, in which both primary and secondary objects are still intact and the sum of their spherical dimensions truly provides the physical HBR. A possible follow-up of the work could be the redefinition of the short-term PoC to circumvent this issue.

3. For a certain combination (i_p, i_f), N_{orb} collision probabilities are obtained ($P^c_{i_p,i_f}\left(\text{TCA}_{i_p,i_f}\right)$). An intuitive approach to locate a potential encounter in time is used: the periodicity and, consequently, the corresponding TCA at which the computed probability is maximum are selected.

4. Overall, $N_p \times N_f$ TCA_{i_p,i_f} are hence obtained, retaining only those "selected" through the maximum PoC criteria.

5. Only the couples mean-covariance corresponding to the selected TCA_{i_p,i_f} are from now on considered.

6. To ultimately determine a single epoch at which the event is estimated to have occurred, a second statistical distance metric is applied. For each combination (i_p, i_f) the Mahalanobis distance is computed between the current parent and fragment GMEs as in Equation 3.2, where the matrices $\boldsymbol{P}$ refer only here to the positional sub-covariance.

$$d_M\left(\text{TCA}_{i_p,i_f}\right) = \left[\left(\boldsymbol{r}^f_{i_f}(\text{TCA}_{i_p,i_f}) - \boldsymbol{r}^p_{i_p}(\text{TCA}_{i_p,i_f})\right)\right]^T [\boldsymbol{P}^p_{i_p}(\text{TCA}_{i_p,i_f}) + ... \\ \boldsymbol{P}^f_{i_f}(\text{TCA}_{i_p,i_f})]^{-1}\left[\left(\boldsymbol{r}^f_{i_f}(\text{TCA}_{i_p,i_f}) - \boldsymbol{r}^p_{i_p}(\text{TCA}_{i_p,i_f})\right)\right] \quad (3.2)$$

7. Of all $N_p \times N_f$ combinations of $d_M\left(\text{TCA}_{i_p,i_f}\right)$, the minimum value is identified. The corresponding $\tilde{i}_p$ and $\tilde{i}_f$ indexes are selected, and the related epoch $\text{TCA}_{\tilde{i}_p,\tilde{i}_f}$ is considered the final estimate $\tilde{t}_0$. Essentially, this is equivalent to obtain a solution of the event epoch which corresponds to the closest distributions from the two mixtures, in terms of position (Figure 3.4).

8. The time error of the estimated solution compared to the "ground-truth", that is, the actual fragmentation epoch (if known), is finally computed as:

$$\varepsilon = |t_0 - \tilde{t}_0| \quad (3.3)$$

where the epochs are usually expressed in ET and in seconds.

Algorithm 3.2 Final TCA selection

Inputs: TCA_{i_p,i_f}, $\boldsymbol{x}^p_{i_p}(\text{TCA}_{i_p,i_f})$, $\boldsymbol{x}^f_{i_f}(\text{TCA}_{i_p,i_f})$, $\boldsymbol{P}^p_{i_p}(\text{TCA}_{i_p,i_f})$, $\boldsymbol{P}^f_{i_f}(\text{TCA}_{i_p,i_f})$, HBR

for $i_p = 1 : N_p$ **do**
  for $i_f = 1 : N_f$ **do**
    for $i = 1 : N_{orb}$ **do**
      Compute P^c at i-th TCA_{i_p,i_f} (Chan, Serra or Alfano)
    end for
    Along the N_{orb} $P^c_{i_p,i_f}\left(\text{TCA}_{i_p,i_f}\right) \rightarrow$ find maximum and corresponding index i_{max}
    Save $\text{TCA}_{i_p,i_f}(i_{max})$
    Save $\boldsymbol{x}^p_{i_p}(\text{TCA}_{i_p,i_f}(i_{max}))$, $\boldsymbol{x}^f_{i_f}(\text{TCA}_{i_p,i_f}(i_{max}))$
    Save $\boldsymbol{P}^p_{i_p}(\text{TCA}_{i_p,i_f}(i_{max}))$, $\boldsymbol{P}^f_{i_f}(\text{TCA}_{i_p,i_f}(i_{max}))$
    Compute Mahalanobis Distance $d_M\left(\text{TCA}_{i_p,i_f}(i_{max})\right)$
  end for
end for
Along the $N_p \times N_f$ values of $d_M\left(\text{TCA}_{i_p,i_f}\right) \rightarrow$ find minimum and select corresponding combination $\left(\tilde{i}_p, \tilde{i}_f\right)$
Obtain final $\tilde{t}_0 = \text{TCA}_{\left(\tilde{i}_p,\tilde{i}_f\right)}$
Compute error ε

3.4. Reliability criterion

As this routine is intended to assist the potential operations following a fragmentation event, a reliability criterion on the estimation has been sought. This allows the routine to provide "alerts" whenever these criteria are not met during any fragment analysis. Thus, the operator could assess whether to request additional observations of the fragment to determine its state more accurately or to focus on searching another object generated by the event for the analysis.

Drawing inspiration from the approach in [12], the criterion of "peak contrast" is applied. In the reference paper this measure serves to determine whether the maneuver detected by the presence of a maximum PoC value has indeed occurred. Similarly, the criterion of maximum PoC applied in this thesis is considered reliable if the "peak" of the collision probability selected as the highest is also distinct from the probabilities computed at other periodicities. In [12], the peak contrast is defined as the logarithmic ratio of the highest

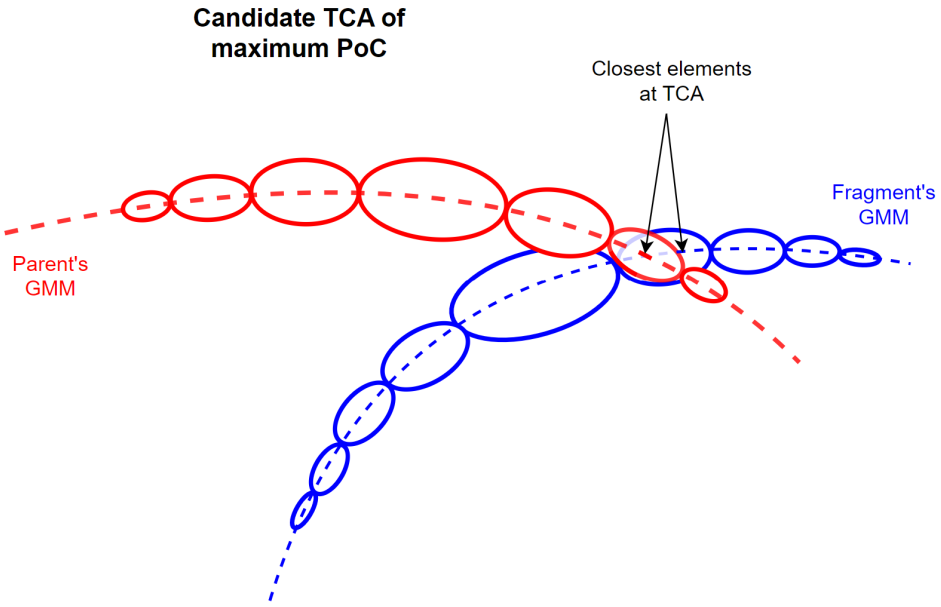

Figure 3.4: Illustration of the GMM sub-Gaussians positional ellipsoids for parent and fragment during an encounter. The Mahalanobis distance metric enables the selection of the epoch associated to the closest elements.

values of encounter probability:

$$P^c_{ratio} = \log_{10}\left(\frac{P^c_1}{P^c_2}\right) \tag{3.4}$$

In the algorithm developed in the thesis, when the maximum PoC value (P^c_1) is determined, the second highest (P^c_2) is also saved. The two values are inserted into Equation 3.4, and if the resulting logarithm is less than a threshold, an alert is generated.
This criterion serves to assess whether, with parent element i_p and fragment element i_f fixed, there is a comparable collision probability at the refined TCAs in two different periodicities. In this case, two situations can arise: the largest PoC is still found at the periodicity where the event occurred, or, due to inaccuracies, the PoC value at a subsequent or preceding periodicity slightly prevails. In the first case, the alert is redundant and serves as a precaution, because the solution converges to the correct periodicity for that fragment. In the second case, the estimated epoch is wrong, however the operator is aware that this may happen.

3.5. Fragment-parent association

The second objective of the routine is to assess whether the observed fragment can be associated to the parent object involved in the event. This addition has been included to enable fragments that "fail" ($\varepsilon > 60$ s) to still be somehow linked to the event that occurred, even though its epoch cannot be accurately determined.
To establish whether an uncatalogued RSO can be correlated with the satellite which broke-up, a measure of cumulative collision probability is employed within the analyzed time window. Specifically, if the probability of at least one encounter occurring within the time span exceeds a certain threshold, then the association is considered positive, regardless of the accuracy of the estimated fragmentation epoch. This measure of the cumulative probability in time is referred to as P^c_{tot}. To evaluate it, the following procedure was developed:

1. The PoC of an encounter at a certain epoch (P^c) is computed.
2. The probability that the encounter considered in step 1 does not occur is computed as $(1 - P^c)$.
3. By repeating point 2 for the all TCAs in the considered time span, and by evaluating their product $\Pi(1 - P^c)$, the probability of no encounters happening within the considered interval is retrieved. This will be referred to as Γ.
4. The probability that at least one encounter between the two objects occurs in the entire span can be now evaluated as $P^c_{tot} = 1 - \Gamma$.

The first step in this sequence of computations involves acquiring a collision probability value for each potential encounter, that is for each candidate refined TCA. To accomplish this and to derive a single probability value for each encounter, Vittaldev's formulation is exploited ([20]):

$$P^c = \sum_{i_p=1}^{N_p} \sum_{i_f=1}^{N_f} \alpha^p_{i_p} \alpha^f_{i_f} \left(f_{lin} \left(\boldsymbol{x}^p_{i_p}(\mathrm{TCA}_{i_p,i_f}), \boldsymbol{P}^p_{i_p}(\mathrm{TCA}_{i_p,i_f}), \boldsymbol{x}^f_{i_f}(\mathrm{TCA}_{i_p,i_f}), \boldsymbol{P}^f_{i_f}(\mathrm{TCA}_{i_p,i_f}), \mathrm{HBR} \right) \right)$$

In order to evaluate an overall PoC when dealing with various elements of the GMM, Vittaldev suggests a double summation over the probabilities computed using any of the linear methods for short-term encounters (f_{lin}). Therefore, Vittaldev's equation is applied to derive the PoC required in point 1, since the possible combinations of probabilities at the relevant TCAs are available. This results in Equation 3.5.

$$P^c = \sum_{i_p=1}^{N_p} \sum_{i_f=1}^{N_f} \alpha_{i_p}^p \alpha_{i_f}^f \left(P_{i_p,i_f}^c \left(\mathrm{TCA}_{i_p,i_f} \right) \right) \tag{3.5}$$

The coefficient $\alpha_{i_p}^p$ and $\alpha_{i_f}^f$ are the weights of the mixtures, derived from the univariate splitting library (Section 3.2). The probability values at TCAs are those computed in Algorithm 3.2. Once the measure of total probability of encounter occurrence (P_{tot}^c) is computed as previously explained, it is compared to a threshold. If P_{tot}^c value falls below the threshold, then the association of the fragment body to the primary object is not positive. Otherwise it may be said that the observed object is a product of the parent break-up. This additional analysis could operationally serve to identify the cloud of debris originating from a specific fragmentation event, subsequently monitor them, predict their future trajectories, and potentially catalog them.
The association procedure is thus included in the routine and its step are summarized in Algorithm 3.3.

Algorithm 3.3 Fragment-parent association

Inputs: $N_{orb} \times N_p \times N_f \; P_{i_p,i_f}^c \left(\mathrm{TCA}_{i_p,i_f} \right)$

Initialize Σ^p as $1 \times N_{orb}$ empty array
for $i_p = 1 : N_p$ **do**
  Initialize Σ^f as $1 \times N_{orb}$ empty array
  for $i_f = 1 : N_f$ **do**
    $\Sigma^f = \Sigma^f + \alpha_{i_p}^p \alpha_{i_f}^f P_{i_p,i_f}^c \left(\mathrm{TCA}_{i_p,i_f} \right)$
  end for
  $\Sigma^p = \Sigma^p + \Sigma^f$
end for
Define $P^c = \Sigma^p$ (array containing N_{orb} PoC values)
Compute $(1 - P^c)_i$, $\forall i = 1 : N_{orb}$
Compute $\Gamma = \prod_{i=1}^{N_{orb}} (1 - P^c)_i$
Compute $P_{tot}^c = 1 - \Gamma$
if $P_{tot}^c > 1e-09$ **then**
  The fragment under analysis derives from the parent object
end if

4 | Test case and Results

This chapter is intended to showcase the outcomes obtained by applying the routine to a test case. The objective is to evaluate its performance and robustness across different propagation models and operational scenarios. All numerical simulations were run in Matlab, together with functions from NASA SPICE Toolkit [40].
Section 4.1 describes the tested fragmentation event, concerning the Russian satellite Cosmos 1408 break-up. Section 4.2 shows how the data set is generated, with focus on the break-up simulation and the detection process. In Section 4.3, the application of the GMM statistical representation is graphically investigated. Additionally, the association of a covariance matrix for the parent object is justified. Section 4.4 evaluates the results for the nominal scenarios. The results of non-nominal conditions are instead investigated in Section 4.5, showing the level of robustness of the routine.
The conditions of the nominal tested scenarios and the sensitivity analyses, as well as the structure in which the results are presented, are intentionally kept similar to what is done in [17], to facilitate the comparison with FRED approach.

4.1. Test case description

A series of simulations have been conducted to test the tools described in Chapter 3, and their results are here presented. The analyzed fragmentation scenario is a past event which involved a kinetic Anti-Satellite (ASAT) test occurred around 02:47 UTC on November 15th, 2021 [41]. This event led to the destruction of a Russian satellite, named Cosmos 1408. Pardini and Anselmo assert in ([42]) that "as of June 20, 2022, the U.S. Space Surveillance Network had catalogued 1764 objects, of which 806 [catalogued] still in orbit". These numbers make this ASAT test the second worst recorded to date.
The orbital elements of Cosmos 1408, that is the parent object, are reported in Table 4.1. The position and velocity state extrapolated from its TLE, input to the simulation, and its corresponding epoch t_{tle}, are reported in Table 4.3. The orbital elements of Cosmos 1408 are reported as well at the epoch of the event (Table 4.2). The analysis time window ranges from t_{tle} up an epoch close to the time when the alert of the event was provided,

that is 06:00 UTC on November 15th.

a [km]	e	i [deg]	Ω [deg]	ω [deg]
6862.2	0.003	82.7	123.4	91.9

Table 4.1: Cosmos 1408 Keplerian elements at t_{tle}.

a [km]	e	i [deg]	Ω [deg]	ω [deg]
6844.7	0.002	82.7	123.3	134.5

Table 4.2: Cosmos 1408 Keplerian elements at 02:47 UTC on November 15th (propagation from t_{tle} through SGP4).

t_{tle}	2021-11-14 23:20:00.00 UTC		
$\boldsymbol{r}^p$ [km]	-3812.229	5692.616	379.691
$\boldsymbol{v}^p$ [km/s]	-0.5645	-0.9086	7.5467

Table 4.3: Cosmos 1408 TLE epoch and corresponding state vector.

4.2. Data set generation

4.2.1. Fragmentation event simulation

Regarding the fragments data, these are first generated by applying the NASA SBM (Section 2.3) to simulate the velocity impulses imparted to the debris. Then an approach follows, which determines the state and covariance of each individual fragment (Section 4.2.2). The former step is summarized here:

1. The parent state vector $\boldsymbol{x}^p = \{\boldsymbol{r}^p, \boldsymbol{v}^p\}^T$, dated at t_{tle}, is propagated up to t_0: 02:47:00.000 UTC on November 15th.
2. The fragmentation event is modelled as a set of impulses applied to the satellite orbital state at t_0, according to Equation 2.3 and to the velocity impulses retrieved from the SBM.

3. A set of 237 fragments is generated in such way. Their Gabbard diagram is reported in Figure 4.1. A representation of their orbits with respect to the parent one is reported in Figure 4.2.

4. At t_0, the pericentre radius of each fragment is evaluated. Those having a pericentre altitude lower than 120 km are discarded because expected to re-enter, and will not be used in the routine testing.

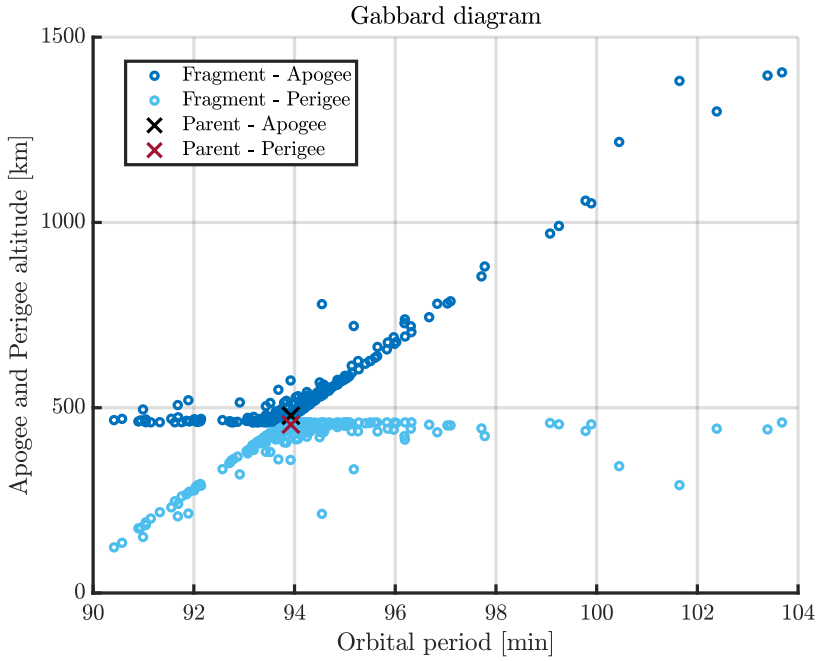

Figure 4.1: Gabbard diagram of the simulated break-up event involving Cosmos 1408.

4.2.2. Fragments detection

The obtained ephemerides of the fragments are propagated until the epoch t_{od} (obtaining $\boldsymbol{x}^f(t_{od})$), when a surveillance radar detection is simulated, and the orbital states and covariance matrices ($\{\boldsymbol{x}^f, \boldsymbol{P}^f\}$) are determined. Nominally, t_{od} is set to 13 hours after the fragmentation event, since this method aims at exploiting a single fragment observation result, available few hours after the event. The approach to simulate the determination process is different depending on the scenario analyzed, and it is described below.

Scenario with no OD error

In this case, a fixed covariance matrix (with standard deviations on position and velocity of respectively $9.32e-05$ km and $1.38e-06$ km/s) is simply associated to all fragments.

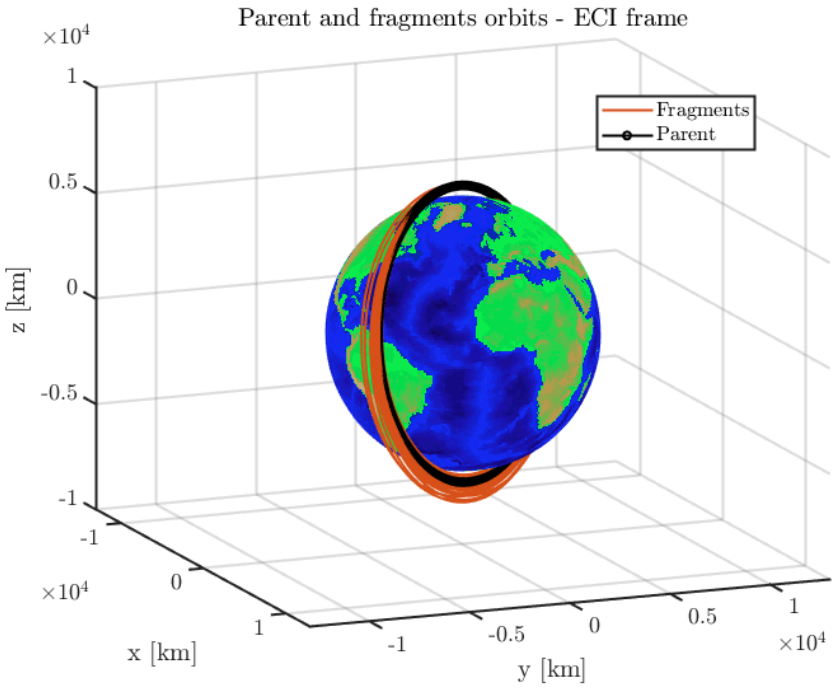

Figure 4.2: Representation of the orbits of parent object and generated fragments, propagated through SGP4 for one period from epoch t_0. Coordinates in ECI frame.

The matrix is derived through the same Initial Orbit Determination (IOD) and Refined Orbit Determination (ROD) approaches detailed below, in paragraph *Scenario with OD error*, setting in this case low values for the measurements noise. This approach results in a small value of the covariance trace, and as a consequence, in positional and velocity uncertainties which are compatible with an IOD process close to being ideal. The final output is a different mean state $\boldsymbol{x}^f$ for each fragment, and a constant covariance matrix $\boldsymbol{P}^f$ for all of them.

Scenario with OD error

In this case, the mentioned radar IOD process is simulated to determine a first guess on state and covariance matrix of each fragment. These results are then refined through a process of ROD. These functions process a set of measurements, perturbed to simulate the presence of a realistic noise introduced by the sensor. A default noise on the range measurement is fixed to 30 m, while the angular noise (equal for both azimuth and elevation) is set to 0.01° in the nominal simulation. The covariance matrix related to the

fictitious ground-station is hence defined:

$$\begin{bmatrix} \sigma_{az}^2 & 0 & 0 \\ 0 & \sigma_{el}^2 & 0 \\ 0 & 0 & \sigma_{ran}^2 \end{bmatrix} = \begin{bmatrix} 0.01^2 & 0 & 0 \\ 0 & 0.01^2 & 0 \\ 0 & 0 & 30^2 \end{bmatrix} \qquad \text{Standard deviations in [deg], [m]}$$

The fragment mean state $\boldsymbol{x}^f(t_{od})$ is propagated in the measurement time window $[t_{od}, t_{od}+$ 30s]. The resulting propagated states are projected in the measurements space to derive a set of simulated angular and range measurements. At this point, the measurements are perturbed, generating random values according to the sensor accuracy covariance. First, the IOD process is applied on them according to [43], and its result is refined through the ROD function presented in [11]. The latter exploits an Unscented Kalman Filter or a-priori least squares depending on the uncertainty covariance resulting from the IOD. The final output is hence a unique couple mean state and uncertainty covariance for each single fragment, both in position and velocity ($\{\boldsymbol{x}^f, \boldsymbol{P}^f\}$).

4.2.3. Other input data

All remaining inputs to run the routine can be therefore defined: the analysis time window ranges from t_{tle} (2021-11-14 23:20:00.000 UTC) to t_a (2021-11-15 06:00:00.000 UTC), the number of GMEs for the parent and fragment objects is set to $N_p = 9$ and $N_f = 9$ respectively, and t_{od} epoch is set to $t_0 + 13$h. The time window is about 6.7 hours long; since the parent orbital period computed at t_{tle} is equal to about 1.6 hours, N_{orb} results equal to 5. Furthermore, the combined HBR is computed as the sum of the parent HBR, which results to be 2.5 m from its radar cross section [44], and of the fragment HBR, set equal to the characteristic length derived from the SBM.
The values set in this work for the thresholds defined in the algorithm are reported as follows. For a single fragment analysis, the result is considered successful if the error in Equation 3.3 is below 60 s. The lower bound of P^c_{ratio}, for the reliability criterion described in Section 3.4, is set equal to 0.6 in the simulations. This value is chosen arbitrarily, considering that "P^c_{ratio} equal to zero leads to two peaks of the same height, while a value $P^c_{ratio} = 1$ represents an encounter probability which is ten times higher than the second highest peak" [12]. Finally, the minimum threshold of P^c_{tot} for a positive fragment-parent association, described in Section 3.5, is set equal to 10^{-9}.

4.3. GMM test case

Before proceeding with the simulations of the various scenarios, the graphical results of the GMM generation for both the parent object and one fragment are reported.
Firstly, as mentioned in Section 3.1, a potential shape for the covariance matrix associated to the parent object at epoch t_{tle} has been investigated. The results of the tested approaches are here reported: in Equation 4.1, the covariance obtained from the very first investigated approach (later discarded) is labelled as $\boldsymbol{P}^p_{old}$, and in Equation 4.2, the covariance obtained from the process inspired by [2], which was subsequently considered more adequate, is named as $\boldsymbol{P}^p$. Indeed, in Section 3.1 it was mentioned that associating a covariance matrix to the parent TLE according to a Flohrer based approach ([1]) for the position and to an isotropic constant value for the velocity was found to be not completely correct, due to the shape of the initial covariance matrix (Equation 4.1) and the corresponding graphical results.

$$\boldsymbol{P}^p_{old} = \begin{bmatrix} 0.0183 & 0.0070 & -0.0217 & 0 & 0 & 0 \\ 0.0070 & 0.0170 & -0.0344 & 0 & 0 & 0 \\ -0.0217 & -0.0344 & 0.3079 & 0 & 0 & 0 \\ 0 & 0 & 0 & 4e-08 & 0 & 0 \\ 0 & 0 & 0 & 0 & 4e-08 & 0 \\ 0 & 0 & 0 & 0 & 0 & 4e-08 \end{bmatrix} \tag{4.1}$$

$$\boldsymbol{P}^p = \begin{bmatrix} 0.0170 & 0.0066 & -0.1434 & -8.75e-05 & 1.33e-04 & -1.37e-05 \\ 0.0066 & 0.0029 & -0.0570 & -3.47e-05 & 5.30e-05 & -5.80e-06 \\ -0.1434 & -0.0570 & 1.2134 & 7.40e-04 & -0.0011 & 1.17e-04 \\ -8.75e-05 & -3.47e-05 & 7.40e-04 & 4.52e-07 & -6.88e-07 & 7.13e-08 \\ 1.33e-04 & 5.30e-05 & -0.0011 & -6.88e-07 & 1.05e-06 & -1.09e-07 \\ -1.37e-05 & -5.80e-06 & 1.17e-04 & 7.13e-08 & -1.09e-07 & 1.16e-08 \end{bmatrix} \tag{4.2}$$

As can be noticed from the shape of $\boldsymbol{P}^p_{old}$ (Equation 4.1), not only the velocity sub-matrix is diagonal, but the positional and velocity uncertainties appear not correlated, due to the extra-diagonal sub-matrices being null.
In Figure 4.3a $10,000$ position samples are illustrated. These are derived from the N_p GMEs distributions of the parent object at epoch t_{tle}, generated via Monte Carlo from the Gaussian covariance $\boldsymbol{P}^p_{old}$ obtained through Flohrer approach. In Figure 4.4a, the samples generated from the same GMEs and propagated through UT (with Keplerian model) are reported (at t_a).

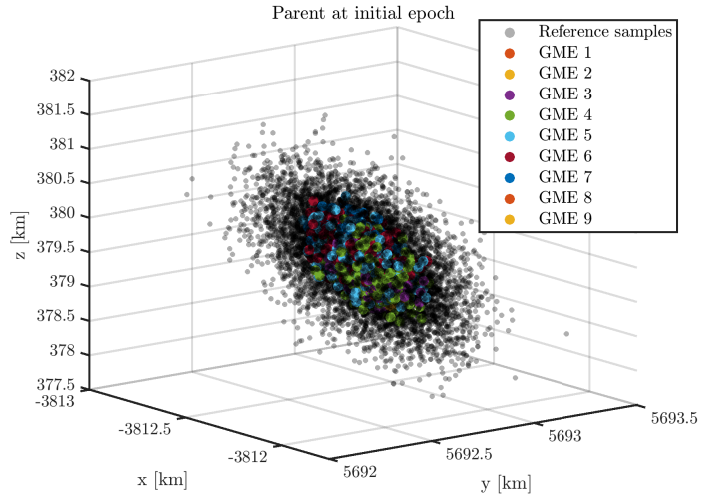

(a) Parent object GMEs at t_{tle}, generated from $\boldsymbol{P}^{p}_{old}$.

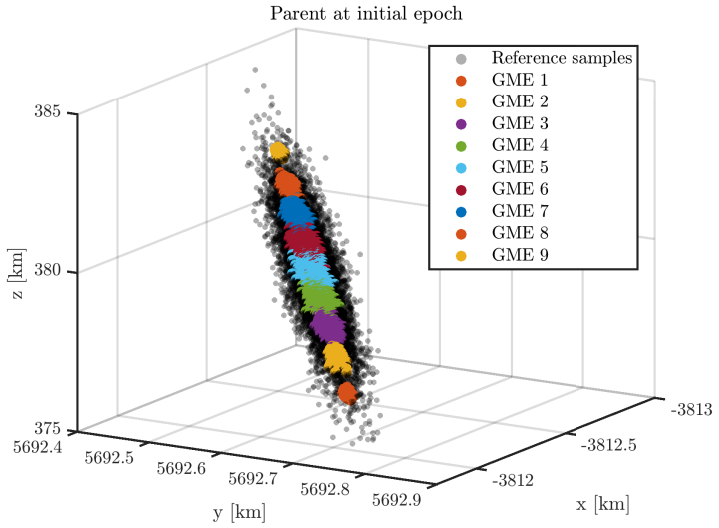

(b) Parent object GMEs at t_{tle}, generated from $\boldsymbol{P}^{p}$.

Figure 4.3: Comparison of different covariance matrices associated to the parent object in terms of splitting approach. Positions in ECI frame.

The same graphs are reported for the GMEs obtained by splitting the covariance matrix $\boldsymbol{P}^{p}$ (see Equation 4.2, Figure 4.3b and Figure 4.4b) associated through the approach described in Section 3.1. It is evident how the splitting direction (as derived in this thesis), works better when applied to the covariance matrix obtained through this method. The samples generated from the splitting applied to $\boldsymbol{P}^{p}_{old}$ (Equation 4.1) do not closely follow the Monte Carlo samples as well as when they derive from $\boldsymbol{P}^{p}$ (Equation 4.2). The shape of the covariance matrix has therefore significant implication on the statistical representation

through GMM. Due to the better behaviour of the uncertainties represented in Figure 4.3b and Figure 4.4b, $\boldsymbol{P}^p$ is then used in the routine as the Gaussian covariance matrix of the parent at t_{tle}.

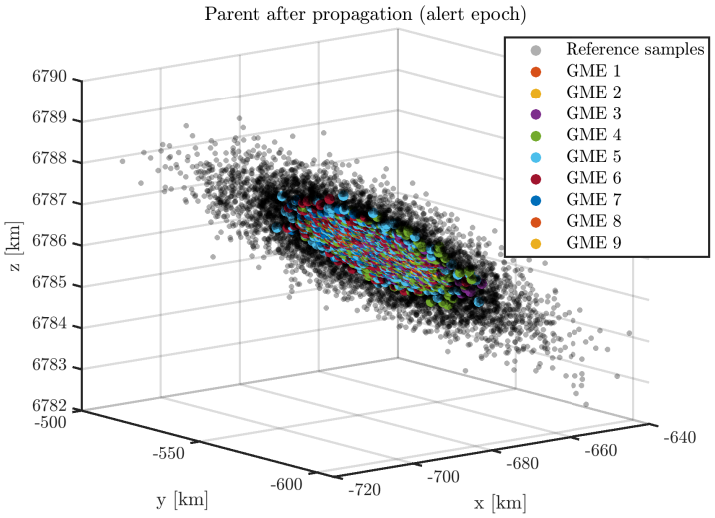

(a) Parent object GMEs at t_a, generated from $\boldsymbol{P}^p_{old}$

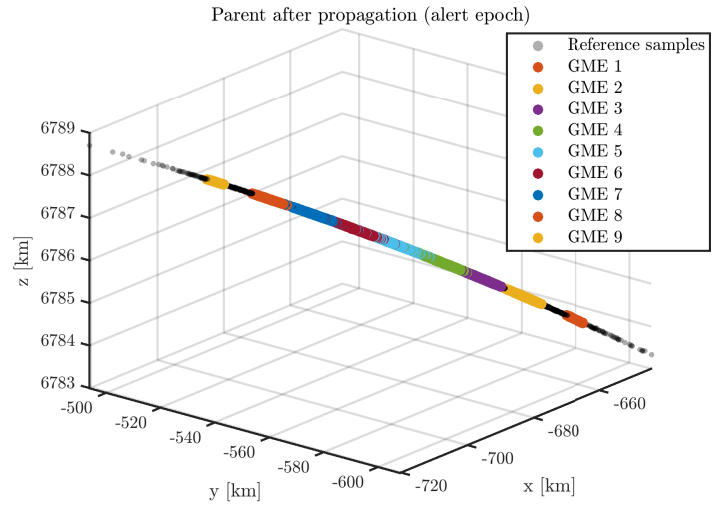

(b) Parent object GMEs at t_a, generated from $\boldsymbol{P}^p$

Figure 4.4: Comparison of different covariance matrices associated to the parent object in terms of splitting approach, after propagation. Positions in ECI frame.

Regarding the GMM generation for the fragments, in Figure 4.5a, 10,000 samples obtained from the positional covariances of the mixture elements of one of the 237 fragments are depicted at OD epoch. The same data are illustrated in Figure 4.5b at epoch t_{tle}, after a backward propagation in time through UT (with Keplerian model). The splitting

approach applied to the distribution generated through the process reported in *Scenario with OD error* (Section 4.2.2) works well for the fragment objects. At the end of the propagation, the elements of the mixture indeed closely follow the slight "banana" shape generated by the dynamics.

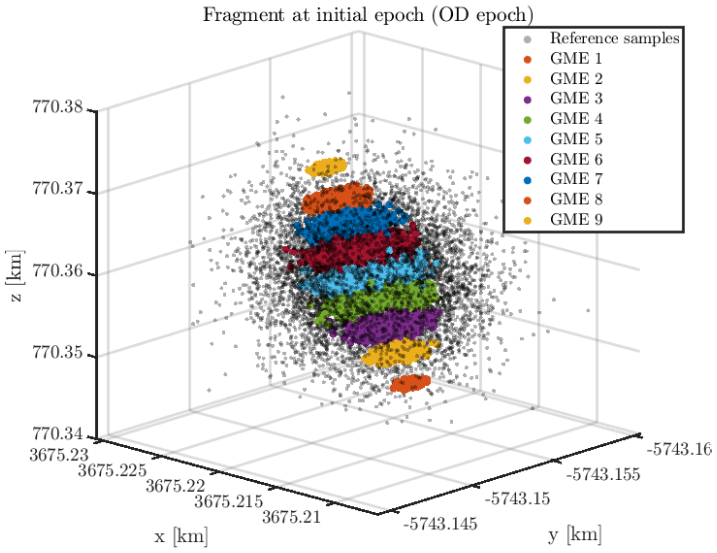

(a) One of the fragments GMEs at t_{od}.

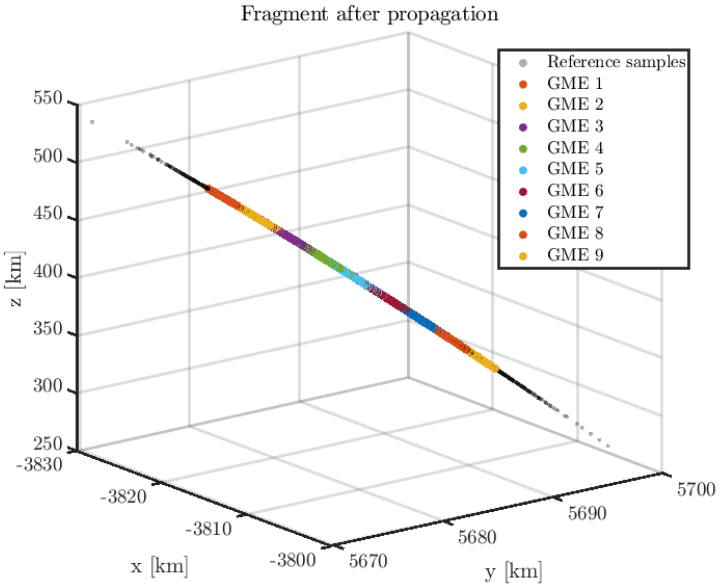

(b) One of the fragments GMEs at t_{tle}.

Figure 4.5: GMEs covariance matrices after splitting of fragment Gaussian covariance. Positions in ECI frame.

4.4. Simulations results

The simulations were run for the whole population of fragments, to allow for straightforward analysis of the results. After each run, a post-process phase is conducted, to analyse the results and generate the plots. Each estimation is considered correct if the error between the estimated epoch and the actual instant of the event is lower than a minute.
For all fragments that do not yield a correct estimation, two categories can be identified:

- Selection failures: this is the case where at least one combination (i_p, i_f) leads to find the highest PoC value outside of the periodicity which includes the event epoch t_0, that is the third one in the simulation. This may result in an error ε larger than half of the parent orbital period, if the combination (i_p, i_f) associated to the minimum Mahalanobis distance is related to an erroneous periodicity. Instead, if this combination (i_p, i_f) is related to the correct periodicity, the error is lower than half of the parent orbital period; however, even this situation is considered a failure related to the selection of the period since, in at least one instance out of all $N_p \times N_f$, the criterion of the highest PoC does not converge to the periodicity of the event.
- TCA failures: this is the case where, even though the convergence to the correct periodicity is always achieved, the error is anyway higher than a minute. This can be attributed exclusively to an estimation of the candidate TCA epochs which is less accurate, and may occur in the MOID computation or in the afterward refinement of the TCAs.

Furthermore, the fragments percentage referred to as "Alerts" is related to those cases where the reliability criterion described in Section 3.4 is not met. Hence in this cases an alert is displayed during the simulations.
Regarding the collision probability computation, Chan's method has always been used for the results reported. Nevertheless, simulations (which are here omitted) were also conducted using the methods of Serra and Alfano. In terms of results, they did not yield any differences.
Finally, it is worth noting that, for the perturbed case, the parameter B^* set to zero is used inside SGP4 both in the generation and detection of the fragments and in the routine.

4.4.1. Unperturbed scenario, no IOD error

As in [17], the unperturbed scenario with no OD orbital state error is tested to assess the theoretical performance of the routine. By "unperturbed," it is meant that the propagation of the objects in time, both in the generation of the data set and within the algorithms of the routine, occurs through an analytical Keplerian model, without the addition of perturbations. For the association of the covariance matrix to the fragments, the approach in *Scenario with no OD error* (Section 4.2.2) is followed before running the simulation.
In this case 229 fragments "survived" the filters on pericenter altitude and on MOID passage epoch. The results in terms of percentages are reported in Table 4.4.

Correct solutions	**Selection failures**	**TCA failures**	**Alerts**
100 %	0 %	0 %	0 %

Table 4.4: Results for the unperturbed scenario with no OD error.

Not alerted simulations	
True negatives	**False negatives**
100 %	0 %

Table 4.5: Results of the reliability alert determined by the P^c_{ratio} criterion, for the unperturbed scenario with no OD error.

All fragments estimate the event epoch with an error of less than a minute. None of the them is alerted, as expected since the whole population gives reliable results, and there are no unwanted "false" alerts produced (indeed in Table 4.5 the "positive" cases are not reported, because non existing). To be specific, a "positive" case occurs when the alert is sent, while "negative" refers to the opposite situation. Additionally, a "true negative" is met when the time error is lower than a minute, and correctly the alert is not triggered. On the contrary, a "false negative" is an erroneous estimation which is however missed by the alert.
The cumulative error ε is reported in absolute value and in seconds (Figure 4.6). The same error values are also showed in terms of percentiles in Table 4.6. These are significantly lower than a minute, with orders of magnitude of the milliseconds in the worst case (100th percentile in Table 4.6). Therefore, under theoretical conditions the method

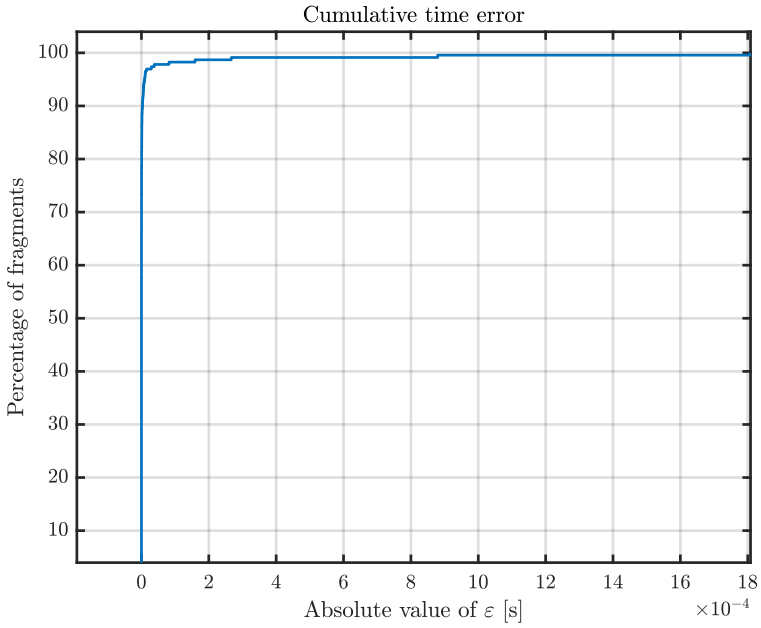

Figure 4.6: Cumulative time error ε in the unperturbed scenario with no OD error.

Percentiles [s]				
5th	**25th**	**50th**	**75th**	**100th**
0	0	0	3.576e-07	0.002

Table 4.6: Time error percentiles in the unperturbed scenario with no OD error.

is highly accurate.

The association process described in Section 3.5 is verified, and is successful for all the simulated fragments. Indeed, in the ideal case the whole population is expected to be correlated to the parent object. Figure 4.7 shows that the association criterion is always met, as $P_{tot}^{c} > 10^{-9}$ for all fragments.

The results of this simulation are in line with an ideal scenario like this. For all 229 fragments, this simulation required a computational time of about 17.5 minutes. This results in approximately 4.6 seconds per fragment, on a single core with Intel(R) Core(TM) i7-8565U CPU @ 1.80GHz 1.99 GHz processor. For the same analysis, FRED algorithm takes 30 seconds per fragment using 1000 samples, demonstrating the advantage of leveraging a statistical representation based on GMM. However, the following analysis was carried out with a deliberately limited number of GMEs compared to the maximum allowed by the univariate splitting library (that is 39). If the number of mixture elements were increased, longer computational times would need to be taken into account.

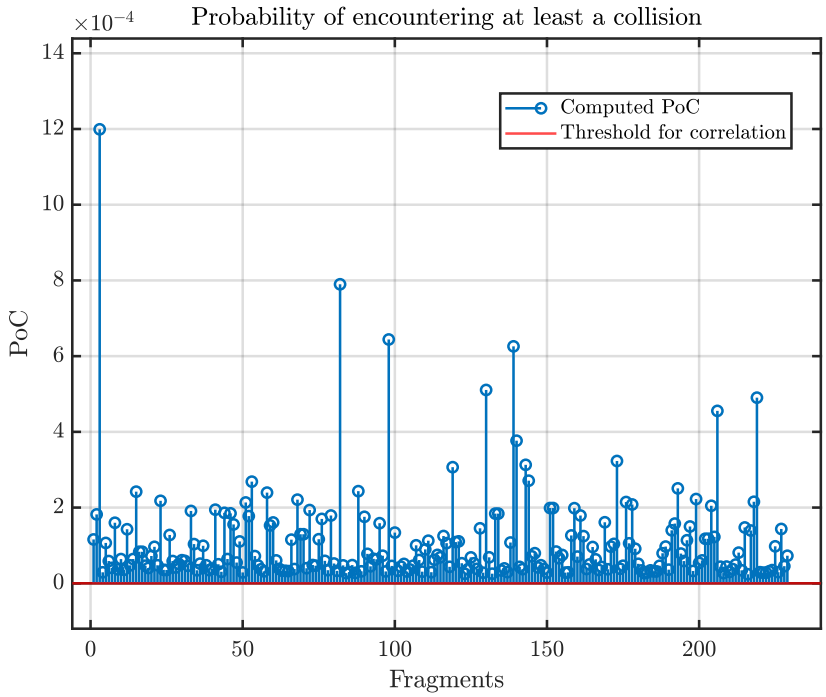

Figure 4.7: Result of the fragment-parent association process in the unperturbed scenario with no OD error.

4.4.2. Perturbed scenario, no IOD error

The analysis is here conducted on a perturbed scenario in which SGP4 is used both in the data set generation, and in the routine itself. This propagation process involves a conversion from Cartesian coordinates to TEME frame at the initial propagation epoch, followed by a subsequent conversion from the obtained SGP4 elements back to Cartesian coordinates at the final epoch. Inside the function which applies this model, these conversions are accomplished using a fixed-point iteration loop, introducing an error that accumulates along the propagation and could potentially impact the outcomes. The effects of these non negligible errors may appear both in the first block, on the results of the MOID passage epochs, as well as in the UP of the covariance matrices, inputs to the PoC evaluation. However, the results of this routine significantly depend on the initial state uncertainty of the fragments. This amplifies through propagation in time, causing the dilution problem (Section 2.4.2), which may negatively impact on the convergence to the correct periodicity through the criterion of maximum PoC.
In the scenario here presented, no error is introduced in the OD, and solutions are correct for all the 226 fragments that passed through the filters (see Table 4.7). The alerts are correctly never triggered, hence no undesired false positive are produced in the output.

Correct solutions	Selection failures	TCA failures	Alerts
100 %	0 %	0 %	0 %

Table 4.7: Results for the perturbed scenario with no OD error.

The reliability criterion results are indeed reported only for the negative cases, in Table 4.8.

Not alerted simulations	
True negatives	**False negatives**
100 %	0 %

Table 4.8: Results of the reliability alert determined by the P^c_{ratio} criterion, for the perturbed scenario with no OD error.

The cumulative error ε is reported in absolute value and in seconds (Figure 4.8). The same error values are also showed in terms of percentiles in Table 4.9. A difference in the orders of magnitude of time errors is observed with respect to Table 4.6, being slightly larger compared to the Keplerian case. This, on the other hand, might be attributed to the numerical errors introduced by the conversion SGP4 -TEME.

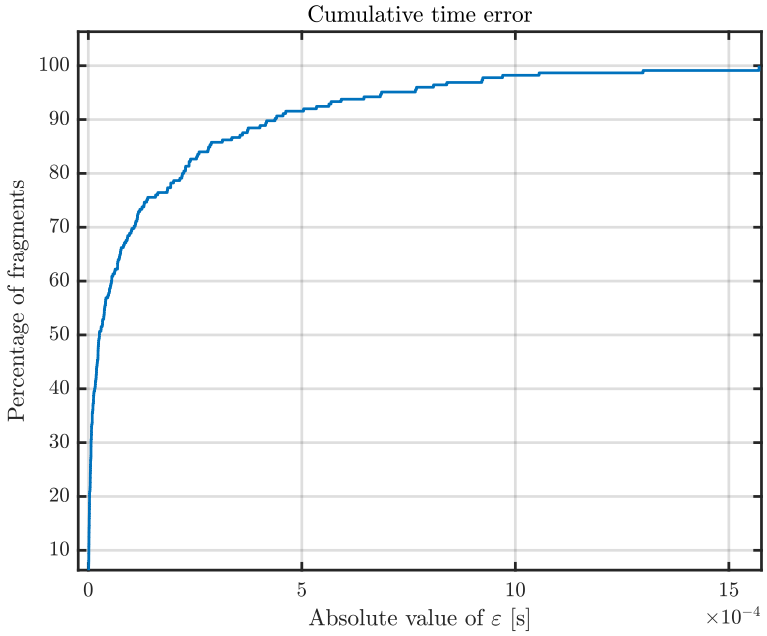

Figure 4.8: Cumulative time error ε in the perturbed scenario with no OD error.

Percentiles [s]				
5th	**25th**	**50th**	**75th**	**100th**
5.961e-07	4.977e-06	2.587e-05	1.374e-04	0.002

Table 4.9: Time error percentiles in the perturbed scenario with no OD error.

The association process presented in Section 3.5 is again successful for all fragments, and the compliance to the P_{tot}^{c} criterion is shown in Figure 4.9.

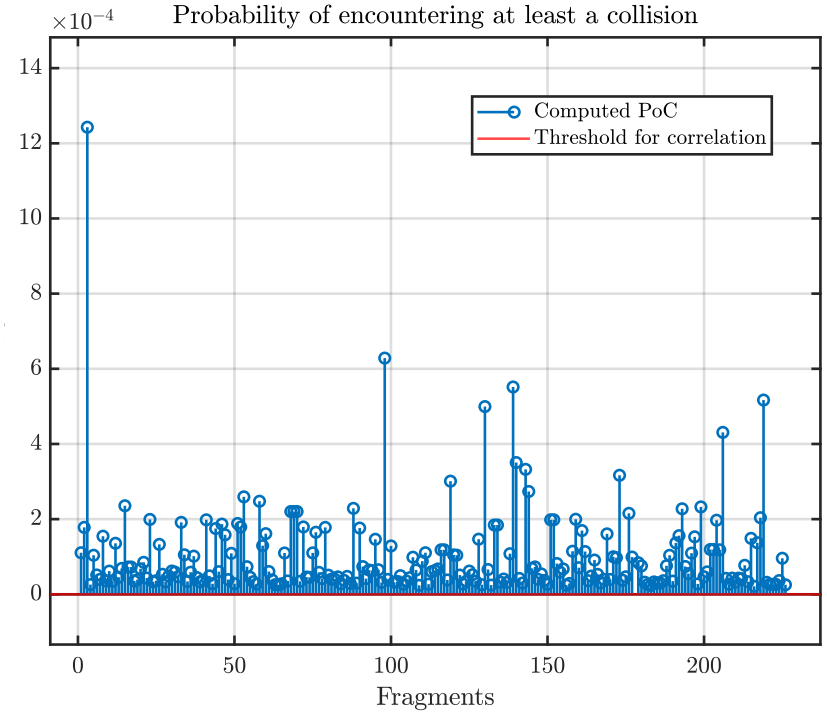

Figure 4.9: Result of the fragment-parent association process in the perturbed scenario with no OD error.

Overall, this simulation required about 3.4 hours, since SGP4 demands more computational time than the Keplerian propagation. This results in approximately 54 seconds required for a single analysis, much faster with respect to the same simulation conducted with FRED, which took about 5 minutes per fragment.

4.4.3. Unperturbed scenario, nominal OD error

The simulations described in Section 4.4.1 and Section 4.4.2 have been performed without introducing any error in the OD process to retain the fragments orbital states. The data

indeed are generated with a simple propagation of the mean states up to a certain epoch, and a subsequent association of a fixed and small covariance matrix. Nonetheless, since the routine shall be tested under conditions that are as representative as possible of an operational scenario, it is necessary to introduce an error. This results in a perturbation of the mean orbital state with respect to the state referred to as ground-truth. Therefore, in the following simulation, the detection of the fragments is performed through the approach described in *Scenario with OD error* (Section 4.2.2), that is introducing an error in the OD process through the measurements noise covariance and the OD process itself. This also results in positional and velocity uncertainties of the covariance matrices in the orders of respectively 10^{-3} km and 10^{-4} km/s, using the Keplerian propagation in the ROD filters. The OD results are then propagated through the unperturbed Keplerian propagator as well.
The results of the simulation are reported in Table 4.10 for the 229 fragments passed to the filters.

Correct solutions	Selection failures	TCA failures	Alerts
82.5 %	17.0 %	0.5 %	5.7 %

Table 4.10: Results for the unperturbed scenario with OD error.

As reported, in the majority of cases, the algorithm successfully converges to the correct solution. Yet, upon comparing results in Table 4.10 with those in Table 4.4, it is evident that the discrepancy introduced in the OD significantly impacts the algorithm performance, particularly in terms of the maximum PoC metric.
The cumulative error ε is reported in absolute value and in minutes (Figure 4.10). The same error values are also showed in terms of percentiles in Table 4.11.

Percentiles [min]				
5th	**25th**	**50th**	**75th**	**100th**
0.006	0.057	0.172	0.532	189.782

Table 4.11: Time error percentiles in the unperturbed scenario with OD error.

The noticeable horizontal jumps in Figure 4.10 correspond to convergence to one or two periodicities prior to or following the third (where the actual event epoch is positioned). For example, the error of 189 minutes reported in the 100th percentile (Table 4.11) is

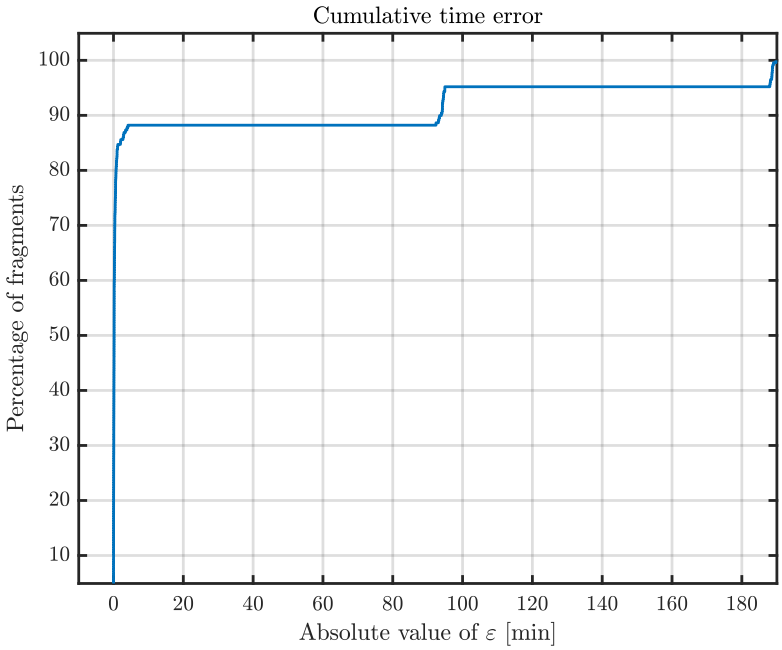

Figure 4.10: Cumulative time error ε in the unperturbed scenario with OD error.

caused by the convergence to a candidate TCA more than 3 hours far from the true epoch, hence in the first or fifth periodicity. Instead, the first visible jump in Figure 4.10, approximately at 100 minutes (one hour and a half), suggests that the solution was found one periodicity prior or after the third one.

As done in [17], an analysis on the Keplerian parameters is conducted to determine if the reciprocal geometry of parent and fragment orbits can be correlated to the estimation error. In particular, it is known that the MOID computation is less stable when the orientations (hence inclination and RAAN) of the fragment and parent orbits are very close each other. This is due to the geometry behind the MOID computation. For this reason, since the fragment orbit is varied from one mean state element of the mixture to another, significant fluctuations in the MOID values may occur. Consequently, even when the final solution converges to the right periodicity, the TCA candidate epochs at that periodicity do not centre around the actual fragmentation epoch, but can be distributed around epochs that are several minutes away. This is due to oscillation in the evaluation of the epochs of passage through the MOID.

The semi-major axis should also affect the results: when it is similar from one orbit to the other, the orbital periods are close as well. This implies that, considering a single combination of parent and fragment mean states of the mixtures, their relative distance from one periodicity to the other does not change significantly. Since the relative distance enters the computation of the collision probability, the PoC values may not vary largely along t_i, triggering the alert effect. In this case, if for any error or due to high positional

uncertainty the computed PoC is slightly higher at the "wrong" periodicity, the solution does not converge close to t_0.
The differences between parent and fragment orbital elements computed at the estimated epoch (for all analysis) are reported in Figure 4.11, versus the time error.

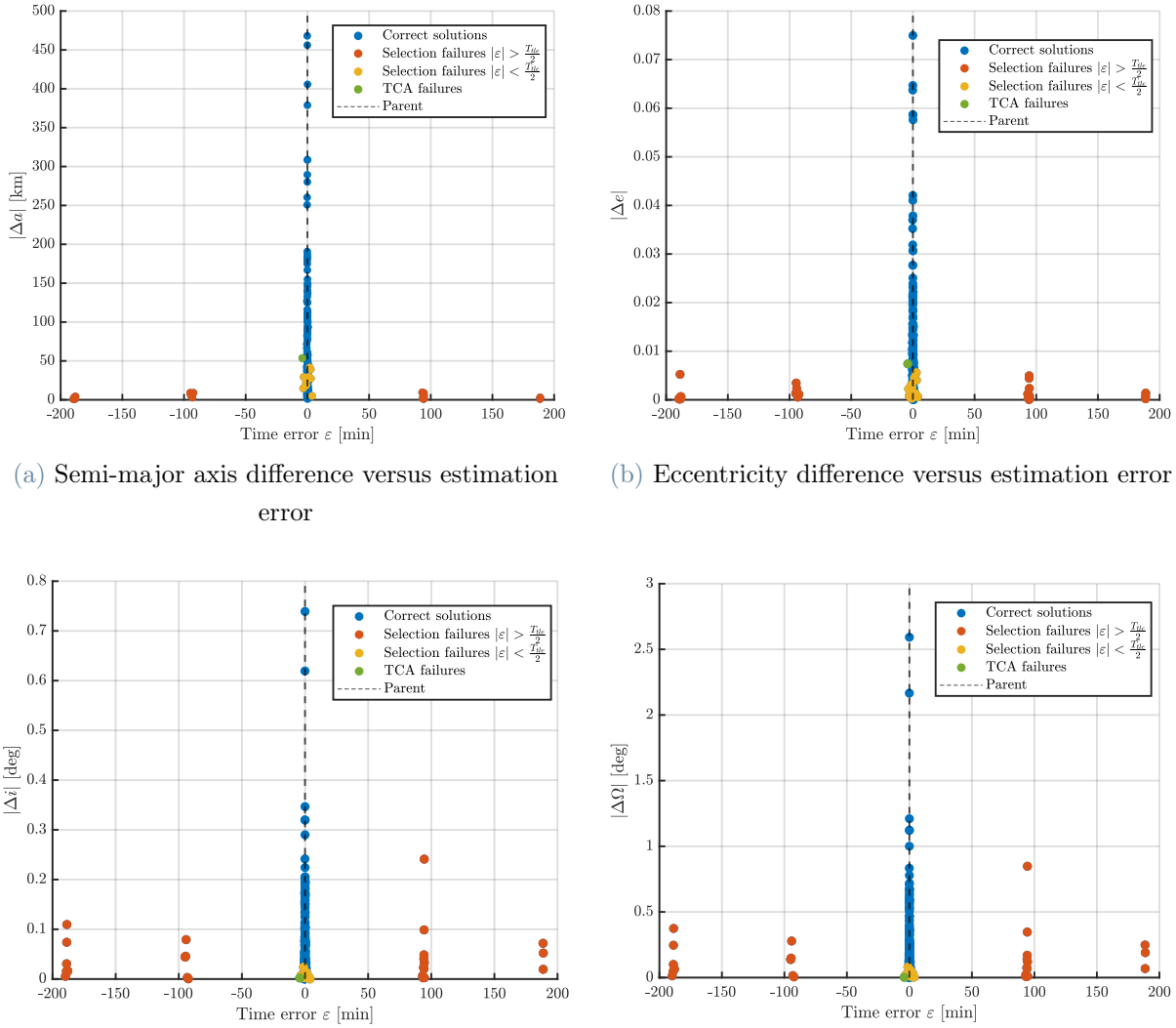

(a) Semi-major axis difference versus estimation error

(b) Eccentricity difference versus estimation error

(c) Inclination difference versus estimation error

(d) RAAN difference versus estimation error

Figure 4.11: Difference between Keplerian elements of the parent and fragment objects versus time error. Results for the unperturbed scenario with OD error.

It can be noticed that significant errors associated with convergence to periodicities other than the third one tend to arise when the parent and fragment orbits have very similar dimensions. On the other hand, errors related to a TCA found within a maximum range of 5 minutes (and in general below half of the parent period) with respect to the actual epoch of the event are more strongly associated with similar values of inclination and RAAN.

These two observations confirm what was mentioned above regarding the geometry of the two orbits and their relationship with the estimation accuracy. It is also worth noting that in the majority of cases labelled as selection failures, the final estimated epoch is associated with an error greater than half of the parent object period. This is because the minimum value of Mahalanobis distance, in this scenario, is found in correspondence of a combination (i_p, i_f) for which the highest PoC criterion failed to converge to the correct periodicity.
Few analyses trigger the reliability alert (Table 4.10), due to a low value of the peak contrast (P^c_{ratio}), related to higher probabilities far from the actual event epoch and consequently, the failure in estimation. Out of all the alerted simulations, the 69.2 % are truly less reliable, leading to a wrong solution and hence defined as "true positives". The rest are instead false alerts, or "false positives". In addition, some of the failed fragments are not flagged, becoming thus false negatives. The specific results of the reliability criterion are reported in Table 4.12.

Alerted simulations		Not alerted simulations	
True positives	**False positives**	**True negatives**	**False negatives**
69.2 %	30.8 %	85.6 %	14.4 %

Table 4.12: Results of the reliability alert determined by the P^c_{ratio} criterion, for the unperturbed scenario with OD error.

Despite the introduced OD errors, the association fragment-parent consistently succeeds, even for fragments that converge to an incorrect solution. Their value of P^c_{tot} always exceeds threshold, as shown in Figure 4.12, with a zoom on the minimum probability computed, related to the analysis n° 96.
For all fragments, this simulation required about 19.4 minutes, similarly to the one in Section 4.4.1.

4.4.4. Perturbed scenario, nominal OD error

To assess the performance of the routine in a realistic scenario, both orbital perturbations and OD errors are introduced in the simulation. Hence, the detection of the fragments is here performed through the approach described in *Scenario with OD error* (Section 4.2.2), however applying SGP4 in the fragments generation, in their detection and in the ROD process.
The corresponding results are reported in Table 4.13 for the 226 fragments passed through

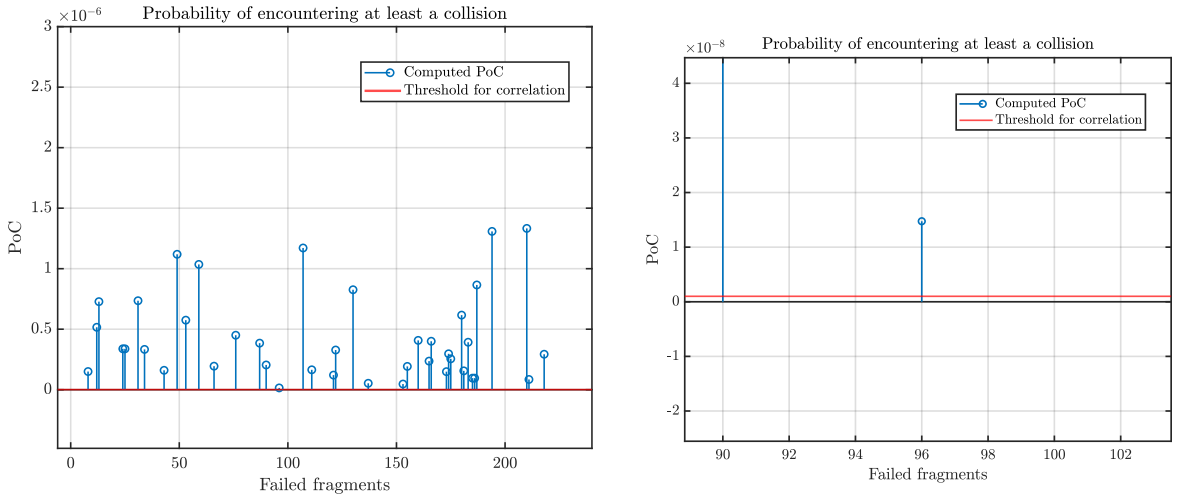

(a) Not zoomed (b) Zoomed

Figure 4.12: Result of the fragment-parent association process in the unperturbed scenario with OD error.

both the pericentre altitude filters and the MOID passage epoch filters.

Correct solutions	Selection failures	TCA failures	Alerts
83.1 %	16.9 %	0 %	5.8 %

Table 4.13: Results for the perturbed scenario with OD error.

Comparing results in Table 4.13 with those in Table 4.7, it appears that, in this case as well, the OD errors affect the algorithm performance, particularly the application of the maximum PoC metric. Indeed, a lower number of analysis converges to a correct solution. Additionally, what explained in Section 4.4.2 is reflected in the results here produced: the numerical errors introduced with SGP4 have a lower impact in the number of correct solutions than the fragments state uncertainties have.
As showed in Table 4.13, the percentage of correct solutions does not worsen with respect to the unperturbed case (Table 4.10). Indeed, it is true that in the perturbed case, errors due to the conversion from SGP4 elements to Keplerian elements are included. However, it could happen that these errors counteract those caused by OD noise. In such case, if the fragment orbital state error resulting from OD leads to the selection of the wrong periodicity through the maximum PoC criterion, SGP4 conversion errors instead could simultaneously correctly guide the algorithm to the correct periodicity.
It is interesting to notice from results in Table 4.13 that there are no failures solely due

to an unstable estimation of the candidate TCA (i.e., TCA failures). All incorrect simulations are, therefore, attributed to a failure of the PoC metric in selecting the correct periodicity, for at least one combination (i_p, i_f) (i.e., selection failures). Among these, as later detailed in the Keplerian parameters analysis (Figure 4.14), most result in an estimated epoch outside of the correct periodicity, due to the contribute of the Mahalanobis distance metric. A lower but still significant number of selection failures tend to produce an inaccurate estimate, however with a lower error (attributed to an unstable computation of the candidate fragmentation epochs) and within the correct periodicity. The cumulative error ε of the estimated epochs is reported in absolute value and in minutes (Figure 4.13). The same error values are also showed in terms of percentiles in Table 4.14.

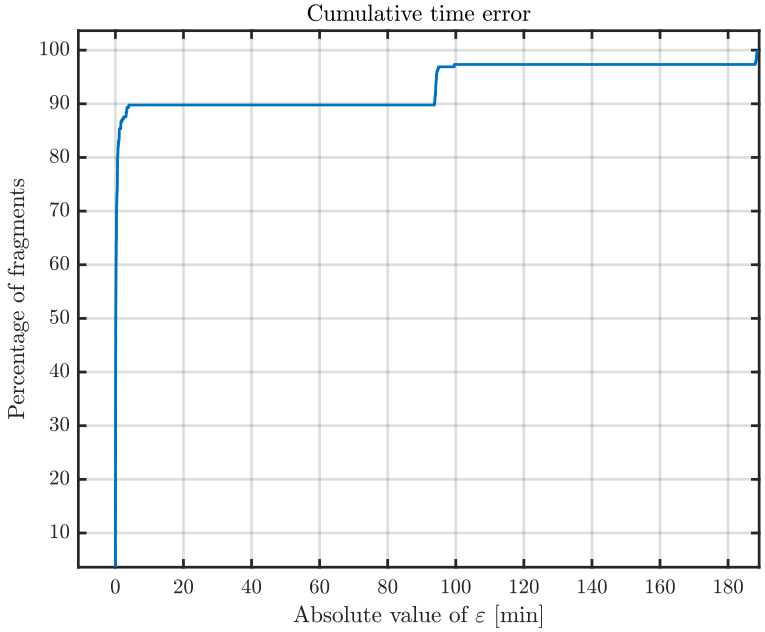

Figure 4.13: Cumulative time error ε in the perturbed scenario with OD error.

Percentiles [min]				
5th	**25th**	**50th**	**75th**	**100th**
0.010	0.050	0.132	0.552	188.559

Table 4.14: Time error percentiles in the perturbed scenario with OD error.

The differences between parent and fragment orbital elements are again reported versus time error in absolute value in Figure 4.14.

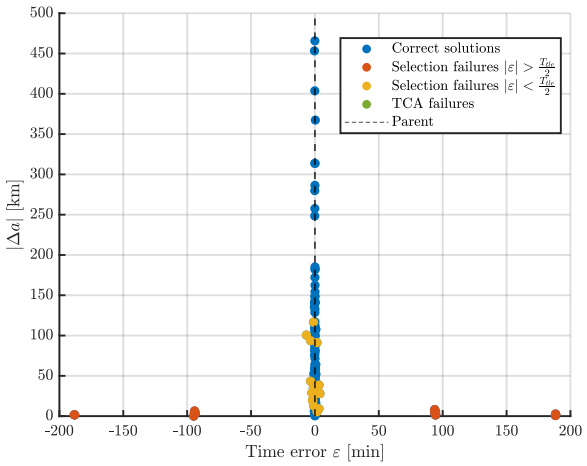

(a) Semi-major axis difference versus estimation error

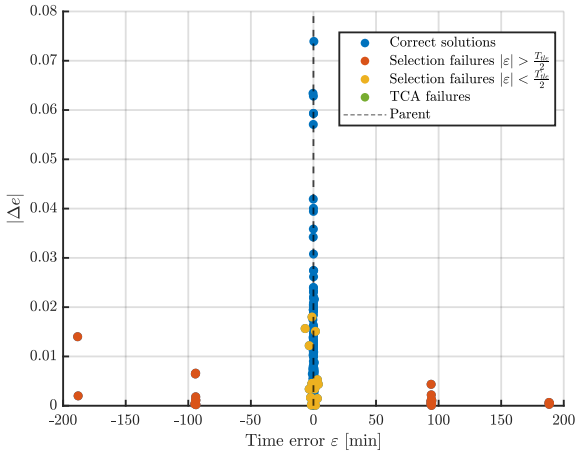

(b) Eccentricity difference versus estimation error

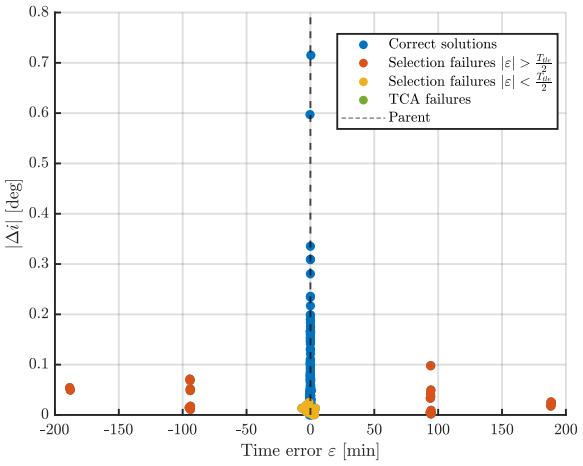

(c) Inclination difference versus estimation error

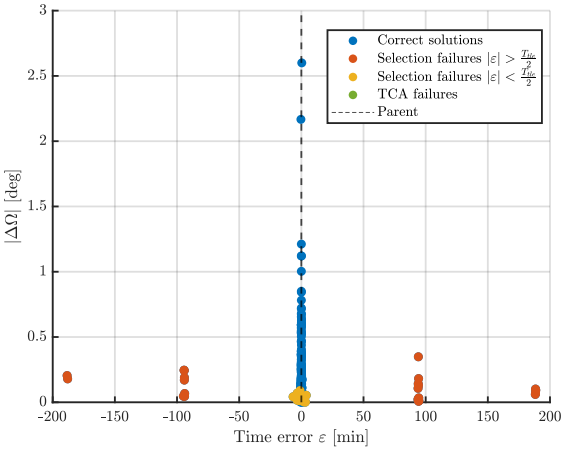

(d) RAAN difference versus estimation error

Figure 4.14: Difference between Keplerian elements of the parent and fragment objects versus time error. Results for the perturbed scenario with OD error.

It can be noticed again that errors produced by an evident convergence to an erroneous periodicity occur at small differences between the dimensions of parent and fragment orbits (Figure 4.14a). On the other hand, when the two orbits have notably similar orientations (Figures 4.14c and 4.14d), this becomes a significant factor contributing to inaccuracies in computing the candidate TCA. As a result, the estimation may deviate by a few minutes from the actual epoch, owing to the MOID calculation instability, despite being correctly located in the third periodicity thanks to the Mahalanobis distance metric. This analysis confirms again that the failure cases are closely related to the mutual geometry of the orbits. Additionally, as mentioned few lines above, in this simulation the failure cases

related exclusively to an inaccurate computation of candidate TCAs do not appear in the results, as well as in Figure 4.14, as can be clearly observed.
Similarly to what happens in Section 4.4.3, few analyses trigger the reliability alert (Table 4.13). Among those, 69.2 % actually provides a non reliable epoch estimation, while the rest are false alerts. The specific results of the reliability criterion are reported in Table 4.15.

Alerted simulations		Not alerted simulations	
True positives	**False positives**	**True negatives**	**False negatives**
69.2 %	30.8 %	86.4 %	13.6 %

Table 4.15: Results of the reliability alert determined by the P^c_{ratio} criterion, for the perturbed scenario with OD error.

It can be observed that the situation of the simulations producing alerts does not change compared to the unperturbed case (Table 4.12). The same percentage is found in both scenarios, both for the simulations that trigger an alert when the estimation is indeed unreliable, and those for which the alert is redundant. Meanwhile, in the case of simulations that do not produce any alert, the 13.6 %, should have actually been reported. Therefore, the reliability criterion for these cases fails, however these are fewer with respect to the scenario presented in Table 4.12.
The results of the fragment-parent association are again reported exclusively for the failed analysis (Figure 4.15), for sake of clarity. The mismatching of the mean orbital state impacts this process as well, since the computation of the parameter P^c_{tot} is in some cases underestimated due to non negligible positional uncertainties inputs to the PoC computation methods. Indeed, not all fragments are in this case correctly associated to the parent object, as shown in Figure 4.15. In particular, the 13.2 % of the incorrect analysis lead also to a cumulative PoC lower than the established threshold. This means that on the overall number of analyzed fragments, the 97.8% correctly achieves the association. Thus, positively, most allow to fully characterize the fragmentation event. However the use of SGP4 impacts negatively on the association algorithm, clearly from the comparison with the unperturbed scenario results (Figure 4.12a).
For all fragments, this simulation required about 3.5 hours, similarly to the case in Section 4.4.2.

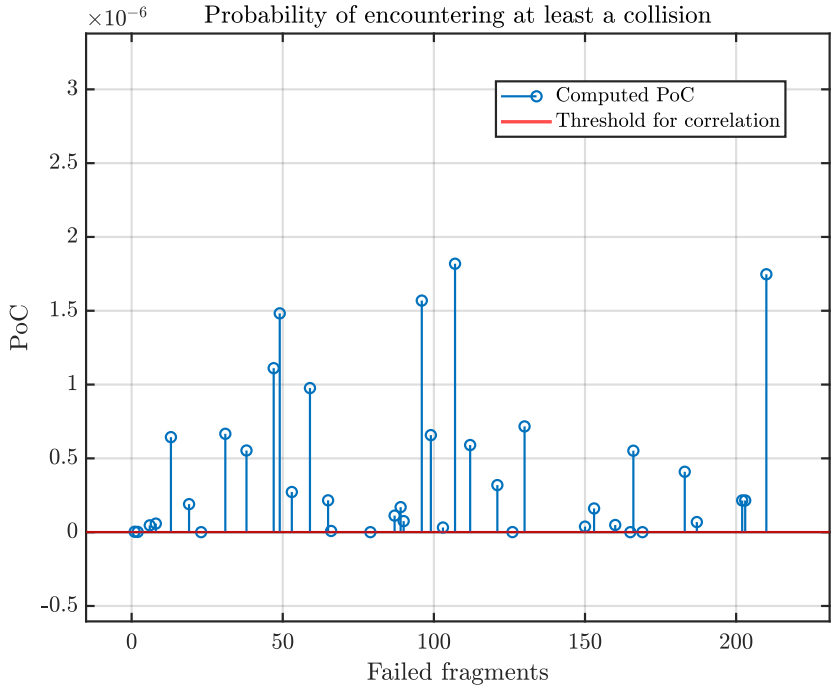

Figure 4.15: Result of the fragment-parent association process in the perturbed scenario with OD error.

4.4.5. Comparison with FRED results

In order to assess the potential of CA techniques as a viable alternative to FRED method, this study compares the performance of different nominal scenarios in terms of estimation accuracy and simulation time.

	FRED	New routine
Correct solutions	92.8 %	100 %
Computational time per fragment	30 s	5 s

Table 4.16: Comparison with FRED: unperturbed scenario with no IOD error.

	FRED	New routine
Correct solutions	90 %	100 %
Computational time per fragment	5 min	54 s

Table 4.17: Comparison with FRED: perturbed scenario with no IOD error.

	FRED	New routine
Correct solutions	68.9 %	83.1 %
Computational time per fragment	5 min	56 s

Table 4.18: Comparison with FRED: perturbed scenario with IOD error.

Comparing Table 4.16, Table 4.17 and Table 4.18 to Table 4.4, Table 4.7 and Table 4.13 respectively, the number of correct solutions is generally higher in the case of the routine developed in this work with respect to those derived through FRED ([17]). Regarding the results of the scenario with OD error, their improvement may be due to the generation of the fragments mean state and covariance, which are obtained through a well-refined ROD, instead of a Keplerian-based method. In the simulations conducted with FRED, the fragment detection is performed using an IOD based on the Siminski approach in [43], which is Keplerian.

4.5. Sensitivity Analysis

Sensitivity analysis are conducted on the perturbed scenario with OD error, to test the robustness of the routine to different conditions. Those that may worsen the results are:

- As in [17], the time elapsed between t_0 and t_{od}: extending the propagation window, the discrepancy at fragmentation epoch for the fragments mean state amplifies.
- As in [17], a larger measurements noise: this causes a higher error in the OD as well as a larger state uncertainties at t_{od}.
- The perturbation of the parent ephemeris, which introduces a further mismatching on the mean state in input.
- The discrepancy of the B* parameter (e.g. due to a different evaluation in the data set generation and in the routine itself).

4.5.1. OD epoch

In all simulations described in Section 4.4, the detection of the fragments is set to happen 13 hours after t_0. Since in an operational context the first detection and OD process might happen later, t_{od} is shifted to two different values: 24 hours and 48 hours after the event. The effect of a larger time elapsed between the event and the OD on the performance is hence investigated.

The results are reported in Table 4.19. It is evident that the more t_{od} is shifted from t_0, the lower becomes the number of fragments leading to a successful solution. As previously mentioned indeed, a longer propagation time implies a higher error on the state vector at t_0. The number of alerts produced in the simulation conducted with +24 h does not vary with respect to the case reported in Table 4.13. On the other hand, in the +48 h case, an increase in the percentage of estimates considered potentially inaccurate appears, possibly following the significant rise of failed solutions.
The OD epoch shifting affects the computational time as well, which increases due to a longer propagation window for the fragments. In this case anyway, the time effort required for the simulation to run on all fragments stays around 3.6 hours, higher but comparable to the case in Section 4.4.4.
To illustrate the convergence to different periodicities, the cumulative errors in absolute value are reported in Figure 4.16a and 4.16b.

Time from t_0	Correct solutions	Selection failures	TCA failures	Alerts
+24 h	73.7 %	26.3 %	0 %	5.8 %
+48 h	56.6 %	42.9 %	0.5 %	8.0 %

Table 4.19: Sensitivity analysis on the OD epoch. Results for the perturbed scenario with nominal OD error.

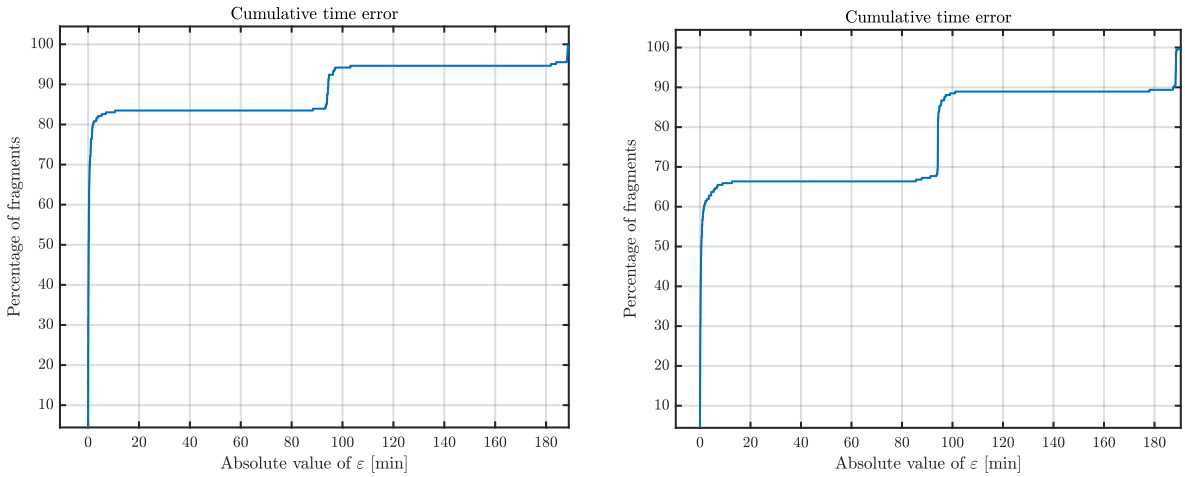

(a) Time from t_0 to t_{od} = 24 h.

(b) Time from t_0 to t_{od} = 48 h.

Figure 4.16: Cumulative time error ε in the perturbed scenario with nominal OD error and variable OD epoch.

The fragment-parent association process is also affected by the increase of elapsed time, as

clearly visible in Figure 4.17a and 4.17b. These illustrate the results of the P_{tot}^{c} evaluation, exclusively for those analysis which lead to a wrong solution, in the +24 h and +48 h cases, respectively. Indeed, displacing more and more the OD epoch, the percentage of simulations achieving correctly the association to the parent object decreases. Specifically, in the +24 h case, the 93.8% of all simulations correctly correlates the corresponding fragment to the event. This percentage is reduced to the 88.0 %, in the +48 h scenario. However, the peak contrast criterion performs well in most cases, allowing still to partially characterize the fragmentation event, although in some cases the epoch detection is not accurate.

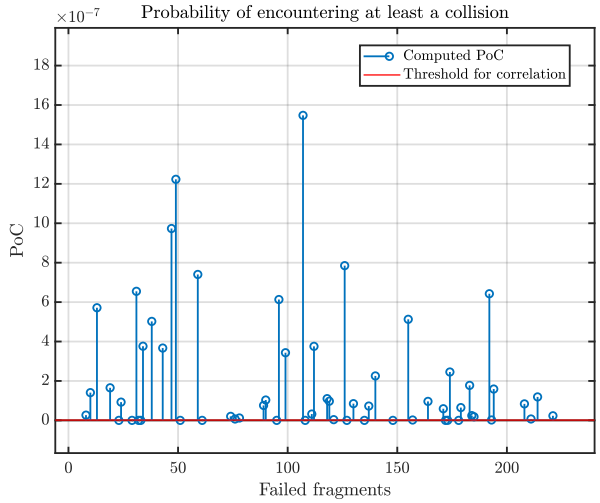

(a) Time from t_0 to t_{od} = 24 h.

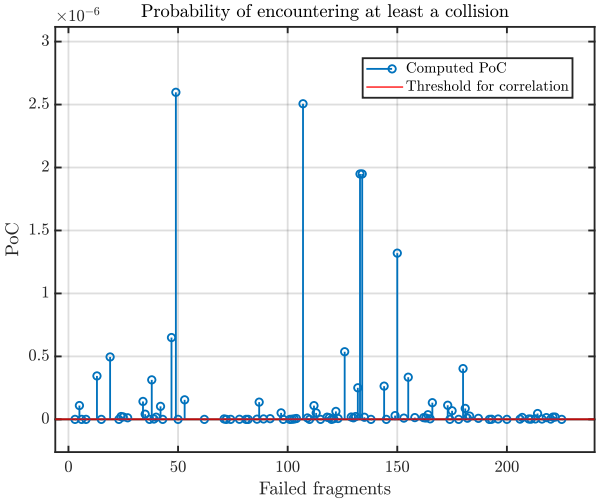

(b) Time from t_0 to t_{od} = 48 h.

Figure 4.17: Results of the fragment-parent association in the perturbed scenario with nominal OD error and variable OD epoch.

Regarding the sensitivity analysis performed using FRED on the same scenario (refer to Table 4.20), it is noteworthy that the new approach presents an increased count of accurate solutions (with respect to Table 4.19). However, it is important to recall the observations detailed in Section 4.4.5: the new improved performance can be attributed to the use of a well-refined ROD, responsible for the higher convergence rates to the correct solution, differently from the Keplerian approach exploited in [17].

Time from t_0	Correct solutions
+24 h	60.8 %
+48 h	43.1 %

Table 4.20: Sensitivity analysis on the IOD epoch conducted with FRED. Results for the perturbed scenario with nominal IOD error. Source: [17].

4.5.2. Measurements noise

As proved by the simulation results presented in Section 4.4, the performance of the routine primarily depends on the accuracy of the OD process. This, in turn, is influenced by factors such as the method used for determination, the length of the observation window, the measurements acquisition frequency, and the quality of these measurements [17]. In particular, a higher noise introduced by the sensor leads to larger uncertainties and discrepancy of the mean state with respect to the real one. Therefore, in this section the robustness of the routine to a larger set of noise input to the fictitious detector is investigated. As surveillance radars tend to have low accuracy in angular track, the noise level for the range is set constant to the nominal value of 30 m. Simultaneously, variations in the angular noise are introduced: from the nominal value of 0.01° to 0.02° and 0.05°. These values are intentionally kept similar to what was done in [17], aiming to facilitate a comparison of the results.
Results are reported in Table 4.21.

Noise	Correct solutions	Selection failures	TCA failures	Alerts
0.02°	77.8 %	21.8 %	0.4 %	9.3 %
0.05°	80.1 %	19.0 %	0.9 %	14.2 %

Table 4.21: Sensitivity analysis on the OD angular measurements noise. Results for the perturbed scenario with OD error.

One can observe that, as the noise associated with the angular track increases with respect to the nominal case (Table 4.13), convergence to the correct solution gets more difficult to achieve, and the percentage of selection failures rises. The number of simulations providing an alert also increases with respect to the nominal case (Table 4.13).
It is interesting to note that in the case of a 0.05° noise, despite it being higher, the routine performs slightly better compared to the case of 0.02° noise. Looking at the higher number of simulations that trigger the alert in the 0.05° noise case (Table 4.21), one could conclude that, in the case of a higher OD error, the PoC computation understandably experiences a greater dilution problem, due to larger uncertainties, which possibly lead to give correct results of cases in which the 0.02° noise scenario failed. The errors related to all estimated epochs are depicted in Figure 4.18a and 4.18b.

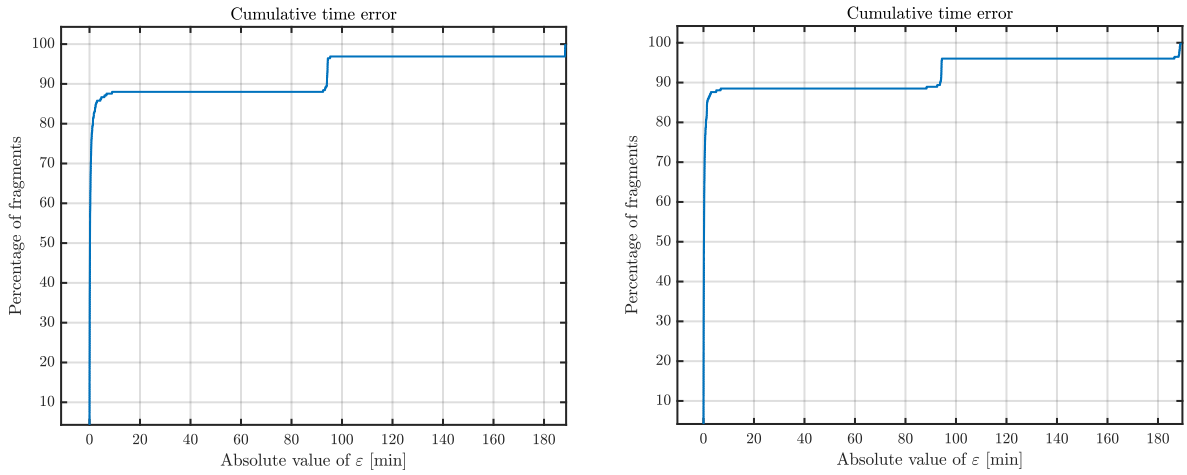

(a) Angular noise: 0.02°.

(b) Angular noise: 0.05°.

Figure 4.18: Cumulative time error ε in the perturbed scenario with variable OD error and nominal OD epoch.

The association process is also affected: with respect to the success rate of case in Section 4.4.4 (97.8 %), here it converges in the 97.3 % of cases for 0.02° noise and again 97.3 % for 0.05° noise. The number of successful associations is still very high, despite many simulations do not lead to a correct estimate. The results of this process are also graphically represented, in Figure 4.19a and 4.19b.
With respect to the same results obtained through FRED, which are reported in Table 4.22, the results presented in Table 4.21 are improved, but once again, the reasons presented so far justify this situation. Indeed, a more accurate ROD process able to include perturbations in the propagation model is used for the new algorithm, with respect to the Keplerian-based IOD applied in [17].

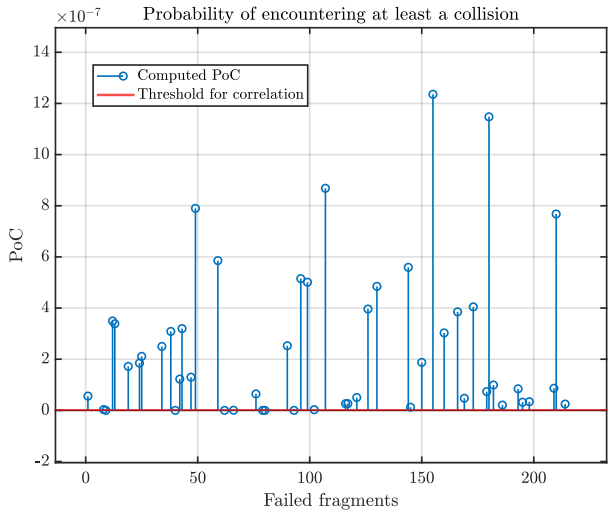

(a) Angular noise: 0.02°.

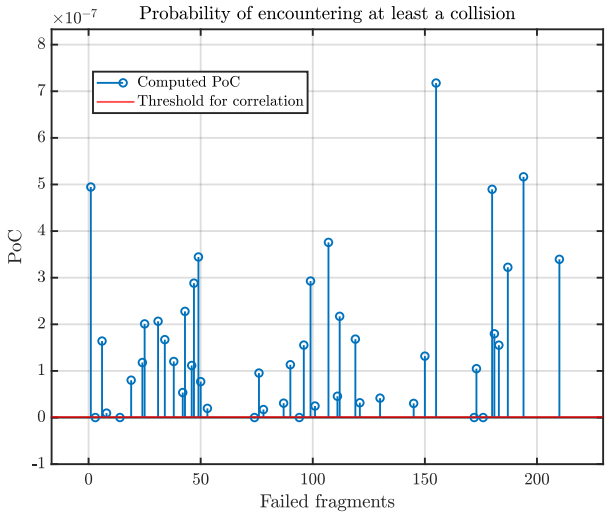

(b) Angular noise: 0.05°.

Figure 4.19: Results of the fragment-parent association in the perturbed scenario with variable OD error and nominal OD epoch.

Noise	Correct solutions
0.02°	66.5 %
0.05°	53.1 %

Table 4.22: Sensitivity analysis on the IOD angular measurement noise conducted with FRED. Results for the perturbed scenario with IOD error. Source: [17].

4.5.3. Parent mean state perturbation

All previous results were obtained exploiting a statistical representation of both objects. However, the mean state of the parent object was never altered with respect to the state acquired from the initial TLE, except during the splitting process required for the GMM generation. However, in real case scenarios, the TLEs are not fully accurate, and differences from the ground-truth shall be considered. Therefore, it is relevant to investigate the implications of a perturbed orbital state of the parent in input to the algorithm.
The mismatch is introduced in the following way:

1. $10,000$ random multivariate samples ($\boldsymbol{x}_s^p$) are generated from the TLE parent state, distributed according to the covariance matrix $\boldsymbol{P}^p$.

2. The perturbed samples are selected according to their statistical distance with respect to the distribution ($\{\boldsymbol{x}^p, \boldsymbol{P}^p\}$), by computing the Mahalanobis distance for each sample:
$$d_M(\boldsymbol{x}_s^p) = \sqrt{(\boldsymbol{x}_s^p - \boldsymbol{x}^p)^T (\boldsymbol{P}^p)^{-1} (\boldsymbol{x}_s^p - \boldsymbol{x}^p)}$$
and by selecting 10 values, going from the lowest to the maximum. The 10 corresponding samples are the only considered from now.

3. 10 simulations of the whole routine are repeated, providing in input as the parent ephemeris each perturbed sample just derived.

The results of the different runs are reported in Tables 4.23 and 4.24. The results on the theoretical scenario (unperturbed case with no error on the IOD) are provided in order to assess the actual implications introduced solely by a perturbed orbital state of the parent object. Each simulation is associated to a different error between the considered parent ephemeris and the ground-truth. The norm of this error is expressed in terms of position and velocity in the results, respectively as ε_r and ε_v. Additionally, columns expressing the percentage of alerts and of successful association between the fragment and the parent, with respect to the ensemble of failed analysis, are reported.
As can be observed from the results presented in Table 4.23, in the theoretical scenario, the mismatching of the input state of the parent object generally leads to a decrease in the number of correct solutions, resulting in a degradation of performance. The reliability criterion is also negatively influenced by the parent state perturbation: in all simulations, only one analysis or even none provide the alert, despite the fact that a non negligible percentage of them returns an inaccurate estimate. Therefore, this criterion appears to be less conservative than it should be. Furthermore, for the least performing simulations,

n°	Correct solutions	Selection failures	TCA failures	Alerts	Successful associations	ε_r [km]	ε_v [km/s]
1	99.1 %	0.9 %	0.0 %	0.0 %	100 %	0.1488	1.58e-04
2	98.3 %	1.7 %	0.0 %	0.0 %	50 %	0.1931	2.12e-04
3	99.6 %	0.4 %	0.0 %	0.0 %	100 %	0.4757	5.30e-04
4	99.6 %	0.4 %	0.0 %	0.0 %	100 %	0.4845	5.38e-04
5	99.6 %	0.4 %	0.0 %	0.0 %	100 %	0.5101	5.71e-04
6	99.6 %	0.4 %	0.0 %	0.0 %	100 %	0.6335	6.93e-04
7	98.3 %	1.7 %	0.0 %	1/229	75 %	0.8047	8.85e-04
8	99.6 %	0.4 %	0.0 %	0.0 %	100 %	1.2844	0.0014
9	90.0 %	10.0 %	0.0 %	1/229	82.6 %	1.6257	0.0018
10	98.7 %	1.3 %	0.0 %	0.0 %	66.7 %	2.8786	0.0032

Table 4.23: Sensitivity analysis on the parent state perturbation. Results for the unperturbed scenario with no OD error.

it occasionally happens that the association fragment-parent fails for some of the failed fragments. Therefore, even this latter process is slightly compromised by having modified the input TLE state. In any case, in this scenario, the results remain good, and the majority of simulations achieve the goal of an accurate estimation of the epoch.
Looking at the results presented in Table 4.24, general trends cannot be identified. In fact, when compared to Table 4.13, it can be observed that for some samples of the original TLE, the routine performs better, while for others, the percentage of correct solutions degrades. This is likely due to the combination of errors introduced by the perturbation of the initial parent ephemeris and those caused by the OD error on the fragments, and by the conversion from SGP4 elements to Cartesian coordinates and back. These factors may indeed influence and compensate each other in a way that is not entirely quantitatively interpretable. It is evident, on the other hand, that in most failed cases the computation of the highest PoC converges to an incorrect periodicity for at least a pair (i_p, i_f), while it occurs less frequently that failures are due exclusively to inaccurate TCAs.
The number of produced alerts (see again Table 4.24) fluctuates but remains in line with the nominal case in Table 4.13. However, it is not possible to define a general trend to relate the increase in the number of successful simulations to the number of produced alerts.

$n°$	Correct solutions	Selection failures	TCA failures	Alerts	Successful associations	ε_r [km]	ε_v [km/s]
1	83.6 %	16.4 %	0.0 %	5.3 %	86.5 %	0.1488	1.58e-04
2	84.0 %	15.6 %	0.4 %	6.6 %	84.2 %	0.1931	2.12e-04
3	84.4 %	15.1 %	0.5 %	5.8 %	82.9 %	0.4757	5.30e-04
4	83.6 %	16.0 %	0.4 %	5.8 %	83.8 %	0.4845	5.38e-04
5	83.1 %	16.9 %	0.0 %	5.3 %	81.6 %	0.5101	5.71e-04
6	84.0 %	16.0 %	0.0 %	6.2 %	83.3 %	0.6335	6.93e-04
7	81.3 %	18.7 %	0.0 %	6.2 %	81 %	0.8047	8.85e-04
8	82.1 %	17.4 %	0.5 %	6.6 %	95 %	1.2844	0.0014
9	83.0 %	16.6 %	0.4 %	5.3 %	97.4 %	1.6257	0.0018
10	75.1 %	24.0 %	0.9 %	6.2 %	68.4 %	2.8786	0.0032

Table 4.24: Sensitivity analysis on the parent state perturbation. Results for the perturbed scenario with nominal OD error and nominal OD epoch.

Finally, one of the analysis conducted on the orbital parameters similarities is illustrated in Figure 4.20. In particular, the results of the 7th simulation of the sensitivity analysis in Table 4.23 are reported, as it is evident here how the situations described in the previous sections unfold. Some fragments, in fact, yield to estimates with errors in the range of tens of minutes, although leading to convergence to the correct periodicity. These are characterized by orbit sizes that are not extremely similar compared to the parent (Figure 4.20a). Meanwhile, their close orientation to the parent orbit causes a slight but not negligible oscillation in the computation of the final epoch (Figure 4.20c and 4.20d).

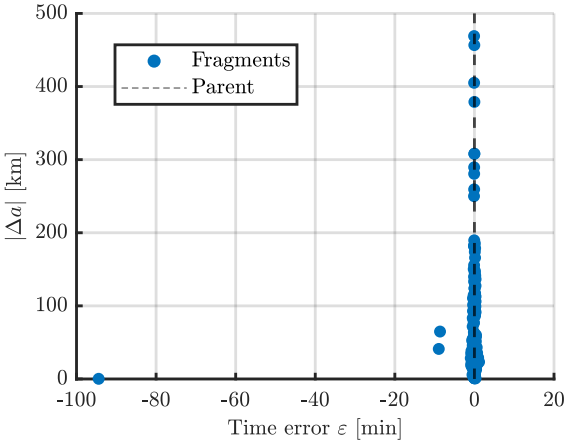

(a) Semi-major axis difference versus estimation error

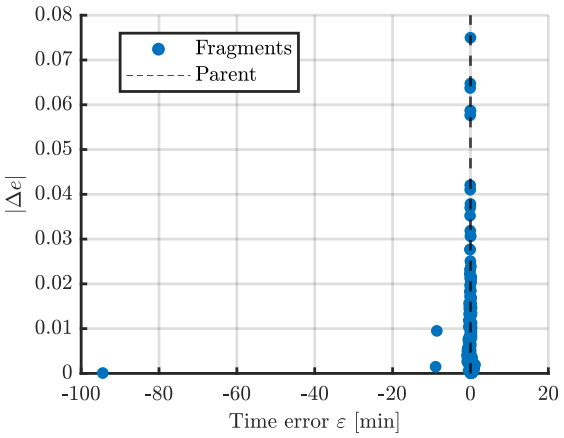

(b) Eccentricity difference versus estimation error

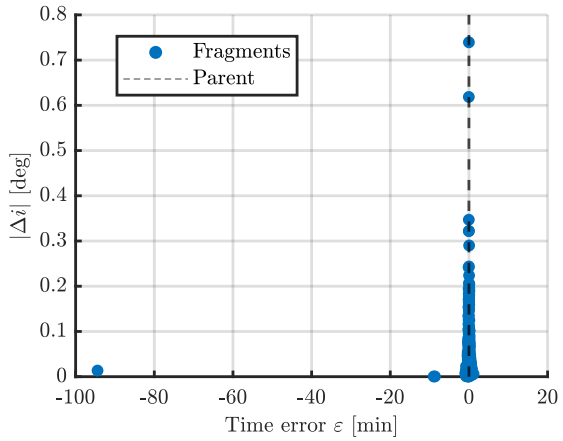

(c) Inclination difference versus estimation error

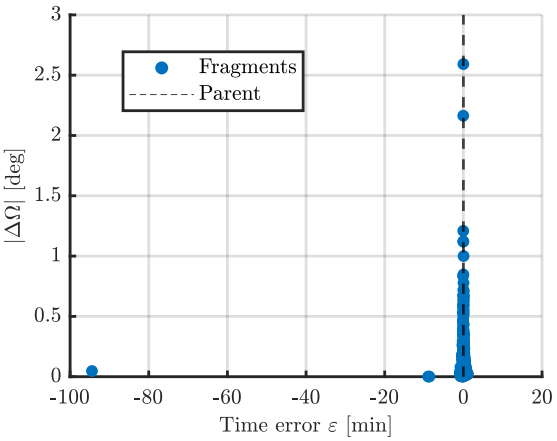

(d) RAAN difference versus estimation error

Figure 4.20: Difference between Keplerian elements of the parent and fragment objects versus time error. Results for the unperturbed scenario with with no OD error and perturbed parent state (7th case in Table 4.23).

4.5.4. Mismatching on B*

In the previous simulations, the same value of the ballistic coefficient B* is used inside SGP4 propagation, both to generate the ground-truth and in the routine itself. Additionally, this value is set equal to zero, both for the parent and fragment, implying that their orbit do not decay. However, given that atmospheric drag plays a crucial role in circularizing and reducing the semi-major axis of LEO orbits, a follow-up simulation of the perturbed scenario is conducted using a more realistic B*. Specifically, a value of 0.00026658 is assigned to the parent object, based on the last available TLE for Cosmos

1408 from Space-Track ([37]), while $B^* = 1e-04$ is assumed for the fragment. These values are set equal both in the data-set generation and in the algorithm. The analysis can be further refined in the future, using the physical parameter estimation procedure presented in [45].
The results are reported in Table 4.25.

Correct solutions	**Selection failures**	**TCA failures**	**Alerts**
82.7 %	16.9 %	0.4 %	6.2 %

Table 4.25: Results for the perturbed scenario with nominal OD error and non null B^*.

Out of the alerted cases (representing the 6.2 % of the data-set), a percentage equal to 78.6 % leads actually to an incorrect solutions. The rest instead are labelled as a false positives. The reliability criterion results are better specified in Table 4.26.

Alerted simulations		Not alerted simulations	
True positives	**False positives**	**True negatives**	**False negatives**
78.6 %	21.4 %	93.9 %	6.1 %

Table 4.26: Results of the reliability alert determined by the P^c_{ratio} criterion, for the perturbed scenario with OD error and non null B^*.

With respect to the nominal case (Table 4.15), the percentage of correctly detected ("true") alerts and non-alerts is interestingly higher. The criterion here detects better unreliable solutions when it should, while a lower number of erroneous estimates are missed.
The results of the fragment-parent association process are illustrated in Figure 4.21 (again for the failed estimations only). A percentage equal to 97.8 % (among the whole population of observed fragments) achieves a successful association, with a value of the cumulative collision probability higher than the required threshold.
Comparing the results in Table 4.25 with those obtained in the case of null B^* (Table 4.13), it can be noticed that the number of simulations converging to the correct solutions decreases. This might be due to addition of the drag perturbation modelling. Instead, it is interesting to note that the percentage of correct fragment-parent associations does not change, remaining consistently high.

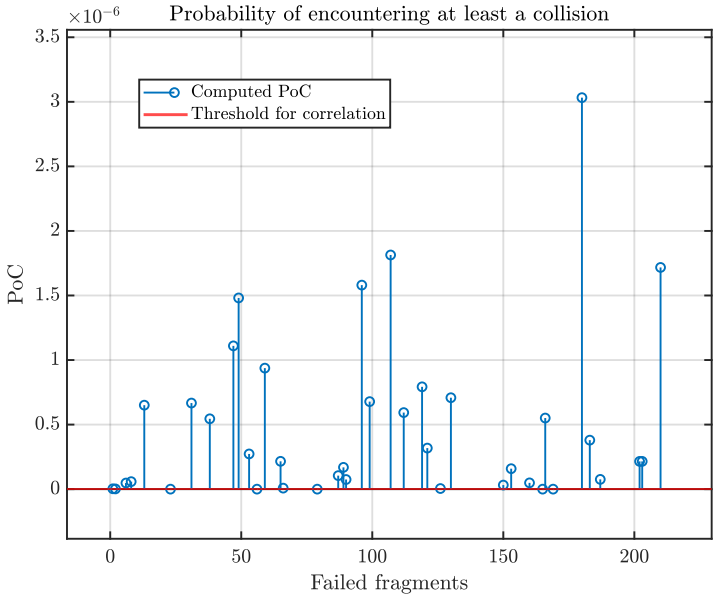

Figure 4.21: Result of the fragment-parent association process in the perturbed scenario with OD error and non null B*.

Additionally, drawing inspiration from [17], an analysis on the mismatching of B* between the ground-truth generation and the routine itself is conducted. This is done since realistically, with the observation of a single fragment, it is not possible to accurately estimate the physical parameters of the object, or it may be necessary to make assumptions about such parameters. Therefore, in the data set generation B* is set as previously to 0.00026658 for the parent and $1e-04$ for the fragment, while in the algorithm both value are modified, by multiplying them times $1e-02$. To assess the robustness of the algorithm to this discrepancy, results reported in Table 4.27 are analysed.

Correct solutions	Selection failures	TCA failures	Alerts
82.2 %	17.3 %	0.5 %	5.8 %

Table 4.27: Results for the perturbed scenario with OD error and mismatching on B*.

Among the alerted simulations (representing the 5.8 % of the data-set) a percentage equal to 84.6 % leads actually to an incorrect solutions. The rest instead is labelled as a false positives. The reliability criterion results are better specified in Table 4.28.

Alerted simulations		Not alerted simulations	
True positives	**False positives**	**True negatives**	**False negatives**
84.6 %	15.4 %	85.9 %	14.1 %

Table 4.28: Results of the reliability alert determined by the P^c_{ratio} criterion in the perturbed scenario with OD error and mismatching on B*.

Looking at Table 4.28, and comparing to the scenario with no mismatching on B* (Table 4.26), the number of wrong solutions which are correctly detected increases. Instead, a higher percentage of non reliable estimates for which the alert is missed can be observed. The results of the fragment-parent association process are illustrated in Figure 4.22, exclusively for the failed simulations.

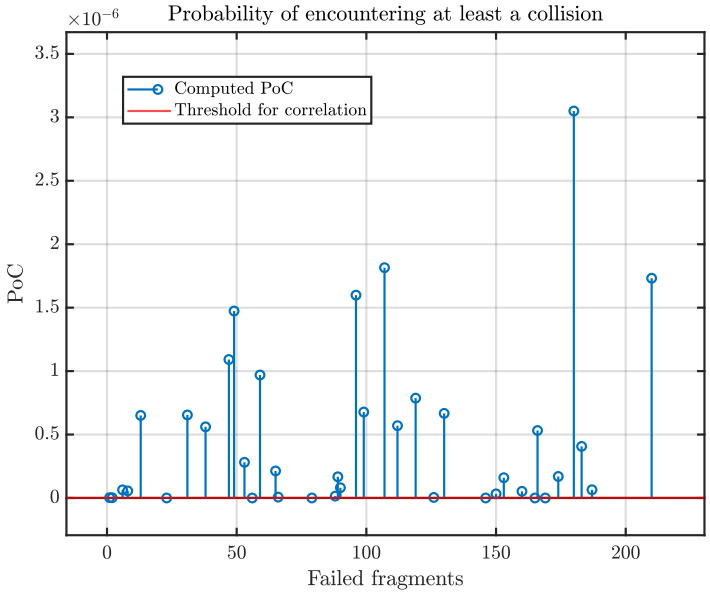

Figure 4.22: Result of the fragment-parent association process in the perturbed scenario with OD error and mismatching on B*.

A percentage equal to 97.3 % (among all simulations) achieves a successful association, with a value of the cumulative collision probability higher than the required threshold. Comparing the results just obtained with those in Table 4.25, it appears that the mismatching on the B* values degrades the number of correct solutions. The percentage of fragments reaching convergence decreases, albeit slightly, but the performance remains robust. However this cannot be considered as a general result, and further simulations should be carried out in the future by varying the B* values differently.

5 | Conclusions and future developments

The thesis presented in this manuscript is intended to contribute to the development of a new routine aimed at characterizing any fragmentation event, under the external conditions typical of a Near-Earth scenario.
The research objectives stated initially have been fulfilled. First of all, the implemented tool is able to detect the epoch of a fragmentation event, given as input a single fragment orbital state and one ephemeris of the fragmented object. Secondly, a criterion for associating the fragment object to the original spacecraft has been implemented to enable a comprehensive characterization of the event. The employed and tested methodologies are based on techniques typical of CA theory. Indeed, the underlying motivation of the conducted work is to search for alternative metrics to rank the candidate fragmentation epochs, with respect to those developed with FRED routine ([17]). The common objective is to estimate the epoch of a fragmentation event through a stochastic approach, ideally applicable within the first few hours following the event alert, in order to mitigate the damage caused by the production and dispersion of debris.
In summary, the work was conducted through the following steps. A comprehensive literature study allowed for the identification of the context in which the new tool could be utilized, the current theories underlying the instruments used to build the algorithm, and finally, the analysis of FRED routine and its performance. The results of these research reviews are reported respectively in Chapter 1, 2, and Section 2.5. Thus, starting from pre-existing knowledge and new insights gained from the literature review, the routine was implemented in its two fundamental blocks: the derivation of candidate TCAs (described in Section 3.3.1) and the ranking of these epochs using collision probability computations (outlined in Section 3.3.2). The second objective of associating the fragment object to the event was then pursued through the implementation described in Section 3.5. The tools built in this manner were then tested through a series of simulations representing both nominal and non-nominal scenarios. To assess the quality of the results, the focus was set on the percentage of analyses that led to a correct solution (within a one-minute

error margin of the actual epoch) as well as the success in the fragment-parent association process. In addition to reporting the results of the new routine, a constant and critical comparison with FRED approaches and performance was conducted. This may serve as foundation for a future tool able to potentially exploit the metrics of both methods together, allowing for an accurate event characterization.

Some significant conclusions can be drawn from the results of simulations and robustness tests:

- The routine operates with a one hundred percent success rate if the scenario conditions are close to being ideal. This implies Keplerian propagation and sufficiently low uncertainty covariance matrix related to the fragments orbital states.
- The results do not experience any degradation when no error is introduced in the OD, despite using a model that includes perturbations. This is a positive outcome; although, as one might expect, numerical errors resulting from the conversion to SGP4 elements are reflected in the epoch estimates. These lead to errors in the order of milliseconds far from the actual epoch, however deviate slightly more than in the Keplerian case.
- In non-theoretical scenarios, the algorithm converges in most cases to the correct solution, but its robustness diminishes when the fragment and parent orbits exhibit similar orientations or have comparable shapes. In particular, when Δa is sufficiently small, convergence to the correct periodicity may more easily fail. Conversely, when orbits have similar inclinations or RAAN, the estimation of candidate epochs may oscillate due to the nature of the MOID computation.
- The result of the MOID computation and the refinement of the passage epochs lead to a very accurate assessment of candidate TCAs, even in cases where the data set is generated with OD errors. Indeed, it results that the majority of failures are attributed to convergence to the wrong periodicity, rather than to an inaccurate evaluation of TCA epochs.
- Convergence to the correct periodicity through the maximum PoC criterion, which in most cases determines a final error of less than a minute, is adversely affected by high uncertainties and errors in the fragment states. This is well observed in the sensitivity analysis conducted on the measurement noise, which degrades the results. However, this is also the result of an increased propagation time window from the event epoch to the detection epoch, which leads to the expansion of errors in the fragment states as well.

- A statistical representation based on GMM is beneficial in terms of computational time. Compared to, for instance, a Monte Carlo approach, the work here conducted allows for a significant speeding up of the analysis on individual fragments.

Future Works

Several developments can be conceived as future extensions of this work.

Certainly, testing different propagation models to introduce additional disturbances or customize their modeling represents a viable direction. Leveraging high-fidelity propagators, for instance the one reported in [46], albeit computationally intensive, promises increased realism of the dynamical environment.

Evaluating the impact of a varying number of GMEs within the mixtures in the routine outcomes holds theoretical interest. A finer discretization of the initial Gaussian distribution into sub-Gaussians theoretically enhances the mixture fitting with the distribution resulting from nonlinear propagation.

The current routine lacks the ability to output statistical information (mean value and standard deviation), due to the use of Mahalanobis distance as a metric for selecting a single final candidate epoch. This limits the error analysis during post-processing, especially for failed simulations. Therefore, a crucial next step involves investigating the determination of meaningful quantities for non-normal distributions, particularly for a set of mixture components, to quantify the uncertainty in the ensemble of TCA combinations. This investigation may necessitate the study of higher-order moments beyond the mean and variance, whose relevance is limited to Gaussian distributions.

Simulation results highlight the critical issue of underestimating collision probability in the presence of high positional uncertainties, negatively affecting the maximum PoC convergence criterion. Consequently, future research may focus on introducing alternative methods of CA that inherently address the dilution problem. Inspiration can be drawn from existing approaches in the literature, including the maximum probability formulation in [31], the Alfriend scale factor in [47], the COPOC approach ([48]) developed by CNES, which employs covariance scaling to manage dilution, and the Kolmogorov-Smirnov test.

As mentioned in Section 4.5.4, a refinement of the B^* sensitivity analysis shall be conducted. The objective would be both to enhance the estimation of the fragments parameter, and to increase the tested cases introducing different levels on the mismatching.

Finally, a significant step entails conducting the fragmentation epoch detection when a fragment is detected by a surveillance sensor, but no OD result can be derived. Indeed, it would be challenging but valuable to define an approach that leads to the epoch estimation directly within the measurement space.

Bibliography

[1] Tim Flohrer, Holger Krag, and Heiner Klinkrad. Assessment and categorization of tle orbit errors for the us ssn catalogue. *risk*, 8(9):10–11, 2008.

[2] Victor P Osweiler. Covariance estimation and autocorrelation of norad two-line element sets. 2006.

[3] Donald J Kessler and Burton G Cour-Palais. Collision frequency of artificial satellites: The creation of a debris belt. *Journal of Geophysical Research: Space Physics*, 83 (A6):2637–2646, 1978.

[4] Nickolay N Smirnov. *Space Debris: Hazard Evaluation and Debris*. CRC Press, 2001.

[5] ESA Space Debris Office. Esa's space environment report 2023. Technical report, ESA ESOC, Robert-Bosch-Strasse 5 D-64293 Darmstadt Germany, 6 2023.

[6] Francesca Ottoboni. Space debris: a growing issue. Liège Université, Master in Aerospace Engineering, 2022.

[7] Space debris by the numbers. `https://www.esa.int/Space_Safety/Space_Debris/Space_debris_by_the_numbers`, . Accessed: 2023-07-07.

[8] Tim Flohrer and Holger Krag. Space surveillance and tracking in esa's ssa programme. In *Proceedings 7th European Conference on Space Debris, Darmstadt, Germany, https://conference. sdo. esoc. esa. int*, volume 1, 2017.

[9] Space surveillance and tracking - sst segment. `https://www.esa.int/Space_Safety/Space_Surveillance_and_Tracking_-_SST_Segment`, . Accessed: 2023-07-08.

[10] A Pastor, J Siminski, G Escribano, M Sanjurjo-Rivo, and D Escobar. Early cataloguing of fragments from break-up events. *Advances in Space Research*, 71(10): 4222–4238, 2023.

[11] Marco Felice Montaruli, Giovanni Purpura, Riccardo Cipollone, Andrea De Vittori, Luca Facchini, Pierluigi Di Lizia, Mauro Massari, Moreno Peroni, Alessandro Panico,

Andrea Cecchini, et al. A software suite for orbit determination in space surveillance and tracking applications. In *9th European Conference for Aerospace Sciences (EUCASS 2022)*, pages 1–12, 2022.

[12] Marcus J Holzinger, Daniel J Scheeres, and Kyle T Alfriend. Object correlation, maneuver detection, and characterization using control distance metrics. *Journal of Guidance, Control, and Dynamics*, 35(4):1312–1325, 2012.

[13] Carmen Pardini and Luciano Anselmo. Review of past on-orbit collisions among cataloged objects and examination of the catastrophic fragmentation concept. *Acta Astronautica*, 100:30–39, 2014.

[14] Roxana Larisa Andrișan, Alina Georgia Ioniță, Raúl Domínguez González, Noelia Sánchez Ortiz, Fernando Pina Caballero, and Holger Krag. Fragmentation event model and assessment tool (fremat) supporting on-orbit fragmentation analysis. In *7th European Conference on Space Debris*, 2016.

[15] Linda Dimare, Stefano Cicalò, Alessandro Rossi, Elisa Maria Alessi, and Giovanni B Valsecchi. In-orbit fragmentation characterization and parent bodies identification by means of orbital distances. In *First International Orbital Debris Conference*, volume 2109, page 6007, 2019.

[16] A Muciaccia, M Romano, C Colombo, et al. Detection and characterisation of in-orbit fragmentations over short and long periods of time. In *INTERNATIONAL ASTRONAUTICAL CONGRESS: IAC PROCEEDINGS*, pages 1–11, 2021.

[17] Marco Felice Montaruli. Multireceiver radar technologies for space surveillance and tracking. 2023.

[18] NASA JPL NAIF. Spice time subsystem. `https://naif.jpl.nasa.gov/pub/naif/toolkit_docs/C/req/time.html`. Accessed: 2023-07-07.

[19] Simon J Julier, Jeffrey K Uhlmann, and Hugh F Durrant-Whyte. A new approach for filtering nonlinear systems. In *Proceedings of 1995 American Control Conference-ACC'95*, volume 3, pages 1628–1632. IEEE, 1995.

[20] Vivek Vittaldev et al. *Uncertainty propagation and conjunction assessment for resident space objects*. PhD thesis, 2015.

[21] Vivek Vittaldev, Ryan P Russell, and Richard Linares. Spacecraft uncertainty propagation using gaussian mixture models and polynomial chaos expansions. *Journal of Guidance, Control, and Dynamics*, 39(12):2615–2626, 2016.

[22] Nicholas L Johnson, Paula H Krisko, J-C Liou, and Phillip D Anz-Meador. Nasa's new breakup model of evolve 4.0. *Advances in Space Research*, 28(9):1377–1384, 2001.

[23] Jia-Sheng Li, Zhen Yang, and Ya-Zhong Luo. A review of space-object collision probability computation methods. *Astrodynamics*, 6(2):95–120, 2022.

[24] Marco Felice Montaruli. Collision risk assessment and collision avoidance maneuver planning.

[25] Romain Serra, Denis Arzelier, Mioara Joldes, Jean-Bernard Lasserre, Aude Rondepierre, and Bruno Salvy. Fast and accurate computation of orbital collision probability for short-term encounters. *Journal of Guidance, Control, and Dynamics*, 39(5): 1009–1021, 2016.

[26] Romain Serra, Denis Arzelier, Mioara Joldes, Jean-Bernard Lasserre, Aude Rondepierre, and Bruno Salvy. Fast and accurate computation of orbital collision probability for short-term encounters. *Journal of Guidance, Control, and Dynamics*, 39(5): 1009–1021, May 2016. ISSN 0731-5090, 1533-3884. doi: 10.2514/1.G001353.

[27] F Kenneth Chan. *Spacecraft collision probability*. American Institute of Aeronautics and Astronautics, Inc., 2008.

[28] Romain Serra, Denis Arzelier, Mioara Joldes, Jean-Bernard Lasserre, Aude Rondepierre, and Bruno Salvy. A new method to compute the probability of collision for short-term space encounters. In *AIAA/AAS Astrodynamics Specialist Conference*, page 4366, 2014.

[29] Ricardo García-Pelayo and Javier Hernando-Ayuso. Series for collision probability in short-encounter model. *Journal of Guidance, Control, and Dynamics*, 39(8):1904–1912, 2016.

[30] XZ Bai and LEI Chen. A rapid algorithm of space debris collision probability based on space compression and infinite series. *Acta Mathematicae Applicatae Sinica*, 32 (2):336–353, 2009.

[31] Salvatore Alfano. A numerical implementation of spherical object collision probability. *The Journal of the Astronautical Sciences*, 53:103–109, 2005.

[32] Salvatore Alfano. Satellite conjunction monte carlo analysis.

[33] James Lee Foster and Herbert S Estes. *A parametric analysis of orbital debris colli-*

sion probability and maneuver rate for space vehicles. NASA, National Aeronautics and Space Administration, Lyndon B. Johnson Space . . . , 1992.

[34] Russell P Patera. General method for calculating satellite collision probability. *Journal of Guidance, Control, and Dynamics*, 24(4):716–722, 2001.

[35] Salvatore Alfano. Relating position uncertainty to maximum conjunction probability. *The Journal of the Astronautical Sciences*, 53(2):193–205, June 2005. ISSN 0021-9142, 2195-0571. doi: 10.1007/BF03546350.

[36] Salvatore Alfano and Daniel Oltrogge. Probability of collision: Valuation, variability, visualization, and validity. *Acta Astronautica*, 148:301–316, 2018.

[37] 18 SDS. Space-track website. `https://www.space-track.org/auth/login`. Accessed: 2023-07-07.

[38] G. F. Gronchi. On the stationary points of the squared distance between two ellipses with a common focus. *SIAM Journal on Scientific Computing*, 24(1):61–80, January 2002. ISSN 1064-8275, 1095-7197. doi: 10.1137/S1064827500374170.

[39] Martin Ester, Hans-Peter Kriegel, Jörg Sander, Xiaowei Xu, et al. A density-based algorithm for discovering clusters in large spatial databases with noise. In *kdd*, volume 96, pages 226–231, 1996.

[40] NASA Jet Propulsion Laboratory. The spice toolkit. URL `https://naif.jpl.nasa.gov/naif/toolkit.html`.

[41] A Muciaccia, L Facchini, MF Montaruli, G Purpura, R Detomaso, C Colombo, M Massari, P Di Lizia, A Di Cecco, L Salotti, et al. Observation and analysis of cosmos 1408 fragmentation. In *INTERNATIONAL ASTRONAUTICAL CONGRESS: IAC PROCEEDINGS*, pages 1–7, 2022.

[42] Carmen Pardini and Luciano Anselmo. The short-term effects of the cosmos 1408 fragmentation on neighboring inhabited space stations and large constellations. *Acta Astronautica*, 210:465–473, 2023. ISSN 0094-5765. doi: https://doi.org/10.1016/j.actaastro.2023.02.043.

[43] Jan Siminski. Techniques for assessing space object cataloguing performance during design of surveillance systems. In *6th International Conference on Astrodynamics Tools and Techniques (ICATT)*, pages 14–17, 2016.

[44] LeoLabs. Analysis of the cosmos 1408 breakup. URL `https://leolabs-space.medium.com/analysis-of-the-cosmos-1408-breakup-71b32de5641f`.

[45] Marco Felice Montaruli, Pierluigi Di Lizia, Emiliano Cordelli, Hélène Ma, and Jan Siminski. A stochastic approach to detect fragmentation epoch from a single fragment orbit determination. *Advances in Space Research*, 72(9):3713–3733, 2023. ISSN 0273-1177. doi: https://doi.org/10.1016/j.asr.2023.08.031. URL `https://www.sciencedirect.com/science/article/pii/S0273117723006798`.

[46] R Cipollone, MF Montaruli, N Faraco, P Di Lizia, M Massari, A De Vittori, M Peroni, A Panico, A Cecchini, et al. A re-entry analysis software module for space surveillance and tracking operations. In *International Astronautical Congress: IAC Proceedings*, pages 1–7, 2022.

[47] Colin Miller. Efforts in solving the dilution problem for orbital collisions.

[48] François Laporte. Jac software, solving conjunction assessment issues. In *Advanced Maui Optical and Space Surveillance Technologies Conference*, page E4, 2014.

A | Appendix A

Algorithm A.1 Chan's PoC computation

Inputs: $\boldsymbol{r}^u_{rel}$, σ^u_x, σ^u_y, HBR

By default $\rho = 0$, $n_{terms} = 10$
$x_m = \boldsymbol{r}^u_{rel}(1)$
$y_m = \boldsymbol{r}^u_{rel}(2)$
$v = \frac{(x_m/\sigma^u_x)^2 + \left(y_m/\sigma^u_y\right)^2 - 2\rho\left(x_m y_m/(\sigma^u_x \sigma^u_y)\right)}{1-\rho^2}$
$u = \frac{\mathrm{HBR}^2}{\left(\sigma^u_x \sigma^u_y \sqrt{1-\rho^2}\right)}$
$m_{vect} = [0 : (n_{terms} - 1) : n_{terms}]$
$P_m = 0$
for $j = 1 : \mathrm{length}(m_{vect})$ **do**
    $m = m_{vect}(j)$
    $k_{vect} = 0 : 1 : m_{vect}(j)$
    $P_k = 0$
    for $w = 1 : \mathrm{length}(k_{vect})$ **do**
        $k = k_{vect}(w)$
        $P_k = P_k + \frac{u^k}{2^k k!}$
    end for
    $P_m = P_m + \left(\frac{v^m}{2^m m!}\right)(1 - \exp(-u/2)P_k)$
end for
$P^c = \exp(-v/2)P_m$

Algorithm A.2 LAAS PoC computation

Inputs: x_m, y_m, σ_x^u, σ_y^u, HBR

By default $n_{terms} = 12$

$p = \exp\left(\frac{(\sigma_x^u)^2+(\sigma_y^u)^2}{4(\sigma_x^u)^2(\sigma_y^u)^2}(-\mathrm{HBR}^2)\right)$

if $\sigma_y^u > \sigma_x^u$ **then**

  $a_- = 1/(\sigma_x^u)^2 - 1/(\sigma_y^u)^2$

  $b_- = x_m^2/(\sigma_x^u)^2 - y_m^2/(\sigma_y^u)^2$

else

  $a_- = -1/(\sigma_x^u)^2 + 1/(\sigma_y^u)^2$

  $b_- = -x_m^2/(\sigma_x^u)^2 + y_m^2/(\sigma_y^u)^2$

end if

$a_+ = 1/(\sigma_x^u)^2 + 1/(\sigma_y^u)^2$

$b_+ = x_m^2/(\sigma_x^u)^2 + y_m^2/(\sigma_y^u)^2$

$c_0 = 0$

$c_1 = 1/(2\sigma_x^u\sigma_y^u)\exp(-b_+/2)$

$c_2 = c_1(a_+b_+ + a_-b_- + 2 * a_+)/16$

$c_3 = c_1\left((a_+b_+ + a_-b_-)^2 + 4(b_+(a_+^2 - a_-^2) + 2a_+^2 + a_-^2)/768\right)$

$c_4 = c_1(a_+b_+ + a_-b_-)^3 + 6a_+(a_+^2b_+^2 - a_-^2b_-^2))/73728 + c_1(\left(-12a_-^2b_+(a_+b_+ + a_-b_-\right) + 12\left(2a_+^3b_+ + 3a_-^3b_- + 4a_+^3 + a_-^2a_+b_+ + 2a_+a_-^2\right))/73728$

$s = c_0 + c_1\mathrm{HBR}^2 + c_2\mathrm{HBR}^4 + c_3\mathrm{HBR}^6 + c_4\mathrm{HBR}^8$

$c_k = c_0$

$c_{k_1} = c_1$

$c_{k_2} = c_2$

$c_{k_3} = c_3$

$c_{k_4} = c_4$

for $k = 0 : n_{terms} - 6$ **do**

  $c_{k_5} = (a_+a_-^4c_k - 2a_-^2(2a_-^2(k+1) + a_+(a_+b_+ + a_-b_-))c_{k_1} - 8a_-(k+2)(2a_+a_-(2k+5) - (2a_+^2b_- + 3a_-a_+b_+ + a_-^2b_-))c_{k_2} + 32(k+3)(k+2)(2a_-^2(2k+5) - (2a_-^2b_+ + 3a_-a_+b_- + a_+^2b_+))c_{k_3} + 128(k+4)(k+3)(k+2)(2a_+(k+4) + a_+b_+ + a_-b_-)c_{k_4})/\left(1024(k+5)(k+3)(k+2)(k+4)^2\right)$

  $s = s + c_{k_5}\mathrm{HBR}^{(2(k+5))}$

  $c_k = c_{k_1}$

  $c_{k_1} = c_{k_2}$

  $c_{k_2} = c_{k_3}$

  $c_{k_3} = c_{k_4}$

  $c_{k_4} = c_{k_5}$

end for

$P^c = ps$

Algorithm A.3 Alfano's PoC computation

Inputs: x_m, y_m, σ_x^u, σ_y^u, HBR

$m = \text{ceil}\left(\frac{5\text{HBR}}{\min(\sigma_x^u, \sigma_y^u, \sqrt{x_m^2+y_m^2})}\right)$

if $m > 100$ **then**

  $m = 100$

end if

$dx = \frac{\text{HBR}}{2m}$

$s_{odd} = 0,\ s_{even} = 0$

for $i = 1 : m$ **do**

  $x = (2i-1)dx - \text{HBR}$

  $y = \sqrt{\text{HBR}^2 - x^2}$

  $s_{odd} = s_{odd} + \left(\text{erf}(\frac{y_m+y}{\sigma_y^u\sqrt{2}}) - \text{erf}(\frac{y_m-y}{\sigma_y^u\sqrt{2}})\right)\left(\exp\frac{-(x_m+x)^2}{2(\sigma_x^u)^2} + \exp\frac{-(x_m-x)^2}{2(\sigma_x^u)^2}\right)$

  if $i \neq m$ **then**

    $x = (2i)dx - \text{HBR}$

    $y = \sqrt{\text{HBR}^2 - x^2}$

    $s_{even} = s_{even} + \left(\text{erf}(\frac{y_m+y}{\sigma_y^u\sqrt{2}}) - \text{erf}(\frac{y_m-y}{\sigma_y^u\sqrt{2}})\right)\left(\exp\frac{-(x_m+x)^2}{2(\sigma_x^u)^2} + \exp\frac{-(x_m-x)^2}{2(\sigma_x^u)^2}\right)$

  end if

end for

$m_{odd} = 4s_{odd}$

$m_{even} = 2s_{even} + 2\left(\text{erf}(\frac{y_m+\text{HBR}}{\sigma_y^u\sqrt{2}}) - \text{erf}(\frac{y_m-\text{HBR}}{\sigma_y^u\sqrt{2}})\right)\left(\exp -\frac{(x_m)^2}{2(\sigma_x^u)^2}\right)$

$x = 0.015dx - \text{HBR}$

$y = \sqrt{\text{HBR}^2 - x^2}$

$m_0 = 2\left(\text{erf}(\frac{y_m+y}{\sigma_y^u\sqrt{2}}) - \text{erf}(\frac{y_m-y}{\sigma_y^u\sqrt{2}})\right)\left(\exp\frac{-(x_m+x)^2}{2(\sigma_x^u)^2} + \exp\frac{-(x_m-x)^2}{2(\sigma_x^u)^2}\right)$

$P^c = \left(\frac{dx}{3\sqrt{8\pi\sigma_x^u}}\right)(m_0 + m_{even} + m_{odd})$